

# STRUCTURAL BOUNDARY DESIGN VIA LEVEL SET AND IMMERSED INTERFACE METHODS

J. A. SETHIAN<sup>†</sup> AND ANDREAS WIEGMANN<sup>†</sup>

DEPARTMENTS OF MATHEMATICS,  
UNIVERSITY OF CALIFORNIA AT BERKELEY  
AND  
LAWRENCE BERKELEY NATIONAL LABORATORY,  
BERKELEY, CA 94720

**ABSTRACT.** We develop and test an algorithmic approach for the boundary design of elastic structures. The goal of our approach is two-fold. First, to develop a method which allows one to rapidly solve the two-dimensional Lamé equations in arbitrary domains and compute for example the stresses, and second, to develop a systematic way of modifying the design towards optimizing chosen properties. At the core, our approach relies on two distinct steps. Given a design, we first apply an Explicit Jump Immersed Interface Method for computing the stresses for a given design shape. We then use a narrow band level set method to perturb this shape and progress towards an improved design.

The equations of 2D linear elastostatics in the displacement formulation on arbitrary domains are solved quickly by domain embedding and the use of fast elastostatic solvers. This effectively reduces the dimensionality of the problem by one. Once the stresses are found, the level set method, which represents the design structure through an embedded implicit function, is used in the second step to alter the shape, with velocities depending on the stresses in the current design. Criteria are provided for advancing the shape in an appropriate direction, and to correct the evolving shape when given constraints are violated.

Submitted for publication, J. Comp. Phys., Nov. 1999

## 1. INTRODUCTION

The goal of this paper is to advance methodology for computing linear elastostatics in complex geometries and to develop techniques for computing improved designs under user-supplied constraints. We present a combined level set and finite difference technique for constructing efficient designs which satisfy certain design criteria. The Explicit Jump Immersed Interface Method is used for computing the solution of the elliptic problem in complex geometries, and the Narrow Band Level Set Method for tracking the motion of the design boundaries under complex speed functions in the presence of topological changes. The application setting for these algorithms is the boundary design of a loaded elastic structure, short structural boundary design. The design changes are based on the weight and stresses, and boundaries are moved, removed or introduced based on these quantities.

By way of illustration, consider a clamped and loaded cantilever (see Figure 1). Suppose our goal is to remove as much material as possible from the original shape, while still making sure that the compliance (defined as the yield under the load) or the maximal stress in the structure stays below a certain threshold value. We can start with the original perforated structure, compute the stress, and then try to add and remove material

---

*Key words and phrases.* Self Design of Elastic Structures, Level Set Method, Explicit Jump Immersed Interface Method, Immersed Interface Method, Linear Elastostatics.

<sup>†</sup>This work was supported by the Office of Science, Office of Advanced Scientific Computing Research, Mathematical, Information and Computational Science Division, Applied Mathematical Sciences Subprogram, of the U.S. Department of Energy under Contract DE-AC03-76SF00098.

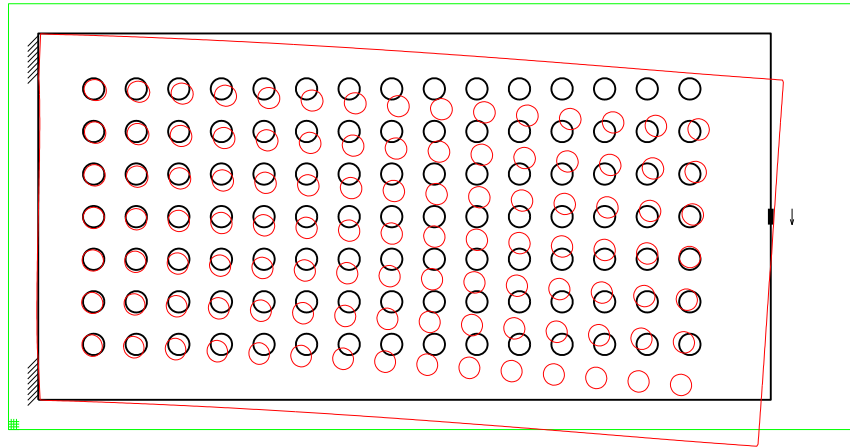


FIGURE 1. *Bending of the initial design of a cantilever with 105 circular holes. Parts of the left boundary are clamped; on the rest of the boundary, including all holes, the traction is specified, with nonzero loading on a small portion about the center of the right boundary. The bending is beyond the regime of small displacement elastostatics and chosen only to illustrate the behavior. The larger rectangle is the computational domain, with a  $320 \times 160$  grid indicated in the lower left corner.*

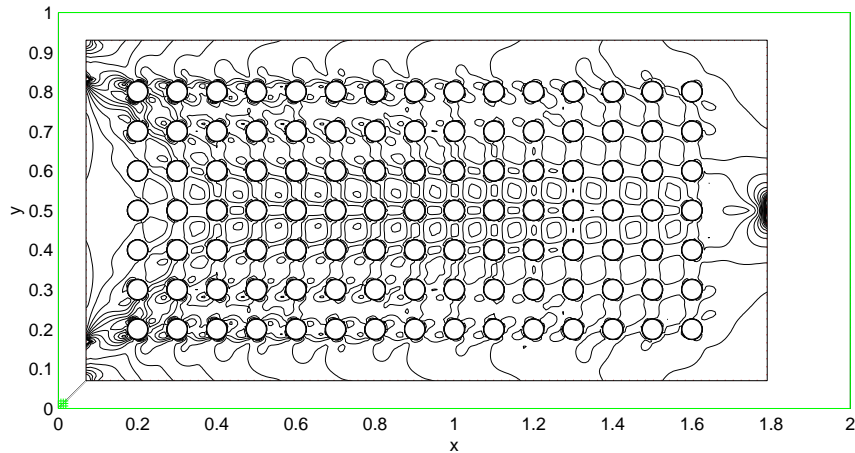


FIGURE 2. *Stress contours on the design from Figure 1.*

in order to reduce the weight in such a way that the compliance or stress do not rise above a given user-prescribed level. Different designs (that is, newly introduced, removed or reshaped holes) will give different compliance and stresses in the design. Our approach is to devise a systematic way to add and remove material. This requires an accurate technique to compute the stresses for a given multiply-connected domain and an accurate technique to remove or reshape existing boundaries and to introduce new ones. The level set method is instrumental in the addition and subtraction of material; the explicit jump immersed interface method is key to compute the stress in arbitrary domains. The improved cantilever that is designed by this procedure looks like Figure 35.

As a general outline, the algorithmic approach presented in this paper is as follows. In the first step, the explicit jump immersed interface method is applied to the equations of 2D linear elastostatics in the displacement formulation (from now on referred to as the Lamé equations), and problems on arbitrary domains are solved quickly and without mesh generation by domain embedding and the use of fast elastostatic solvers. This effectively reduces the dimensionality of the problem by one. In the second step, the given design is modified. The level set method, which represents the design structure through an embedded implicit function, is used to alter the shape, with velocities depending on the stresses in the current design. These stresses can be found from the displacements that were found in the first step. Criteria are provided for advancing the shape in an appropriate direction, and to correct the evolving shape when given constraints are violated. The two steps are iterated until no more improvement can be made.

The benefit of using the explicit jump immersed interface method is to avoid mesh generation and the use of fast elastostatic solvers; the benefit of using a level set method is the elegant handling of changes in topology such as merging of holes, or filling in of holes with large stresses around them.

The application of the algorithmic methodology presented in this paper is by no means complete. Our techniques allow for accurate and efficient computation of the linear elastic equations for arbitrary geometry, and provide an approach to alter the design shape in a systematic way to satisfy user-prescribed constraints. As such, the application falls under the category of a constrained minimization problem. As with many such problems, our technique allows us to improve the objective, but cannot be guaranteed to find the global minimum. In particular, our criteria for perturbing the given design and searching for nearby trial shapes which both satisfy the constraint and contain less material is somewhat ad-hoc; we can neither prove that it converges, nor guarantee that it extracts the global minimum. Nonetheless, it provides an appealing way to approach some of these problems.

## 2. BACKGROUND ON STRUCTURAL BOUNDARY DESIGN AND PREVIOUS WORK

One main approach to structural design for variable topologies is the method of *homogenization* [8, 5, 6]. The following summary is paraphrased from [3]. *Homogenization extracts homogeneous effective parameters from heterogeneous media. The effective properties of a composite material are defined as the homogenized coefficients of a fine mixture of given phases. The difficult “layout” problem of material distribution is replaced by a much easier “sizing” problem for the density and effective properties of a perforated composite material obtained by cutting small holes in the original homogeneous material.* Work in homogenization has shown that at low volume fraction the optimal solution for perforated plates in plane stress and bending, respectively, tends to that of least-weight trusses and grillages (see [4, 7]).

From our point of view, the most important insight obtained by homogenization is that some objectives in the mathematical modelling of structural design are oversimplified and do not yield the intended results. The objective “to minimize a weighted sum of compliance and weight for a given load” results in designs with infinitesimal especially shaped pores in the material that make the structure not manufacturable and make the structure very sensitive to variations in the loading. In practical situations, one would like the material to be comprised of macroscopic solid and void regions, allow for variations in the loading and has to account for cost of manufacturing, etc. Homogenization can deal with these issues by penalization of intermediate densities and postprocessing, but the attractive conceptual simplicity of the homogenization approach is lost for realistic requirements.

In the “evolutionary structural optimization” approach of Xie and Steven, [36], changes in size, shape and topology of the structure are achieved by removing elements (usually referred to as *hard kill*) from some fixed finite element discretization of a “ground structure”, an initial large domain in which the final designed domain is *a priori* known to

be contained. The weight reduction can be governed by the stress, stiffness, frequency or buckling load. In the similar “reverse adaptivity” approach of Reynolds et. al. [20], approximately fully stressed structures are found by removing a fixed percentage of relatively understressed material. Reverse adaptivity refines finite element meshes near the boundary during the design procedure to reduce computational cost or increase resolution. Essentially, both evolutionary structural optimization and reverse adaptivity are homotopy methods, the difference (apart from the adaptive mesh refinement in reverse adaptivity) is that the parameter is a percentage of stress or a percentage of weight.

Another related approach is the “bubble method” of Eschenauer and Schumacher [12, 13], where the topology is modified in a prescribed fashion by placing holes of known shape at optimal positions in the structure, based on so-called characteristic functions of the stresses, strains and displacements. From this method we have gathered the importance of letting the design for a given topology “settle into a good shape” before further changing the topology.

Sharp boundary-based methods for structural design are a more direct approach than homogenization. For example, they do not require the reformulation of the constrained problem via Lagrange multipliers, and in general allow the modeller more explicitly account for any features she wants to incorporate into the design. The possible complications make the notion of proving the optimality of the design hopeless, but it may be argued (as, for example, in [20]) that for many applications, optimality is not as useful a concept as improvement, and we will thus only make claims for our own method regarding the latter. As in [20], “we improve the design by making more efficient use of the material”.

### 3. OVERVIEW OF WORK AND ALGORITHMIC APPROACH

Adopting the principal idea of redesigning the structure based on the distribution of stresses in the current design to find fully stressed structures, we focus on the resolution of the boundaries. The level set method [18], introduced by Osher and Sethian, is designed for moving boundaries with changes in topology. In our case, the velocity of this boundary motion depends on the stress on the boundary. On arbitrary domains we obtain the stresses by solving the linear elastostatic equations in the displacement formulation and differencing the displacements using the Explicit Jump Immersed Interface Method (see [35]), a finite difference technique on uniform grids after Li and LeVeque’s Immersed Interface Method (IIM, [14]) that is capable of dealing with non grid-aligned boundaries with the same truncation error as interior differences. The biggest benefit of our approach compared to the earlier work [36, 20] is that it is easier to add material (with some subgrid resolution) at hole boundaries with high stress than on a triangulated finite element mesh. In particular, this allows us to start with designs that have holes cut “in the wrong place”, and see these holes disappear.

In the elliptic portion of structural boundary design, mesh generation for the design domains can become the major cost. We avoid the mesh generation step by separating the representation of the boundary from the uniform computational grid. To keep the data structures simple and in order to use fast elastostatic solvers on rectangular domains [33], the problem is posed on a larger, rectangular domain  $R$  with zero normal boundary conditions. The boundary conditions on the original boundary are rewritten as jump conditions that introduce discontinuities in the displacements inside  $R$ . Our choice of jump and boundary conditions forces the extended solution to vanish on the extension but to match the solution inside the structure. On the level of the linear algebra, a Schur-complement reduces the number of variables from proportional to the grid points to proportional to the length of the boundary normalized by the mesh width.

In the design portion of structural boundary design, changes in topology provide the greatest challenge. The structure boundaries are viewed as moving, holes may merge with each other or the exterior or may have to be newly created. The level set method represents the boundaries implicitly as the zero level curve of a grid function that is essentially the

distance from the boundary. Boundary motion and merging as well as the introduction of new holes are all performed using this grid function. This approach also allows the detection of regions that have become separated from the nontrivial boundary conditions and have to be dropped from the computations. For efficiency reasons, we use the narrow band level set method (see [1]).

We considered two options for the boundary velocity. The first is derived from the stress on the boundaries and inside the structure. The second is based on the stress on the boundaries only, and then extends the velocity onto the grid by constant values in the normal direction. We use the second option because the first does not allow for addition of material and because in our experience tended to give undesirable corners in the boundary geometry. In addition, the second option theoretically maintains a distance function from the zero contour.

In more detail, the elliptic aspects of structural boundary design are considered in §4 while the design aspects are treated in §5. To compute the stresses, we *derive jump conditions* from given displacement boundary conditions in §4.1, and from given traction boundary conditions in §4.2. The separate treatment of boundary conditions serves only to illustrate the concepts; in the numerical examples in §6, different types of boundary conditions are given on the same component of a boundary. We use a weighted least squares approach for derivative estimation (see §4.3) which is similar to ideas in Li [15] and improve and implement the corrections for cross-derivatives (previously described in [35]) in §4.4. Derivative estimation and corrections are for the first time carried out to third order for the purpose of achieving an  $\mathcal{O}(h^2)$  truncation error at all points, including points neighboring the boundary. §4.5 briefly describes the Schur-complement approach for embedded irregular domains and §4.6 summarizes the ideas behind the fast elastostatic solver.

In §5, we review the narrow band level set method for front propagation in §5.1 before going into its extensions (e. g. determination of the boundary velocity) to structural boundary design in §5.2. Some remarks concerning the explicit jump immersed interface method for varying geometries follow in §5.3.

We demonstrate second order convergence of the explicit jump immersed interface method for elastostatics in §6.1. The third order approximations improve the solutions to be less sensitive to changes in the boundary geometry. Second order convergence of the displacements gives first order convergence of the stresses. These are again extrapolated to the boundaries using a weighted least squares fit in order to find the front velocities as required by the Level Set method.

In §6.2, we show that we can solve elastostatic problems in irregular regions with the same  $\mathcal{O}(N \log N)$  efficiency that the fast solver exhibits for rectangular domains, and that it is feasible to solve medium-sized problems of up to 1.6 million variables on workstations.

In the examples of structural boundary design in §6.3, the idea is to reduce the weight of the structure while keeping the compliance below a certain bound and achieving as uniform a stress distribution as possible in the structure, i.e. to find so called *fully stressed structures*. We can start from a ground structure like [36, 20], but any existing design may be improved — or found to be unimprovable — with our approach. Three mechanisms enable changes in the size, shape and topology of the structure. We introduce new holes by cutting away material along contour lines of the von Mises stress. A homotopy parameter called the removal rate ([36]) guides the choice of contour levels. The removal rate is a percentage of the maximum von Mises stress in the original design, and is slowly increased according to another parameter, the evolutionary rate, to remove material from the structure. We then move the boundaries using a level set method with velocities given from the stress on the boundaries and by extending these velocities from the boundaries by a constant value normal to the boundaries, as suggested in [2]. The procedure stops

when it cannot further decrease the weight of the structure without “constraint violation”. Alternatively, an observer may want to choose the best design out of the sequence of designs.

## 4. FINITE DIFFERENCES FOR THE LAMÉ EQUATIONS IN GENERAL DOMAINS

Recall the two-dimensional Lamé equations:  $\mathbf{u} = (u, v)$  are the displacements in  $x$  and  $y$ , respectively, and

$$\begin{aligned} -\mu(\Delta u + u_{xx} + v_{xy}) - \lambda(u_{xx} + v_{xy}) &= f^u \text{ in } \Omega, \\ -\mu(\Delta v + u_{xy} + v_{yy}) - \lambda(u_{xy} + v_{yy}) &= f^v \text{ in } \Omega. \end{aligned}$$

Here  $\mu$  and  $\lambda$  are the Lamé constants,  $\mathbf{f} = (f^u, f^v)$  are body forces, and  $\Omega$  is an open, connected but not necessarily simply connected domain. We will also write (with  $C = \mu/(\mu + \lambda)$ ),

$$C\Delta u + u_{xx} + v_{xy} = -\frac{f^u}{\mu + \lambda} \text{ in } \Omega, \quad (1)$$

$$C\Delta v + u_{xy} + v_{yy} = -\frac{f^v}{\mu + \lambda} \text{ in } \Omega. \quad (2)$$

Displacement boundary conditions are

$$\mathbf{u} = \bar{\mathbf{u}} \text{ on } \Gamma_1 \subset \partial\Omega, \quad (3)$$

Here  $\bar{\mathbf{u}} = (\bar{u}, \bar{v})^T$  are given functions on  $\Gamma_1$ , the part of  $\partial\Omega$ , the boundary of  $\Omega$ , where displacements are given. Traction boundary conditions are

$$\boldsymbol{\sigma}(\mathbf{u})\mathbf{n} = \mathbf{g} \text{ on } \Gamma_2 \subset \partial\Omega. \quad (4)$$

We assume that the coefficients, geometry and boundary values are such that the problem (1)–(4) has a unique solution.

Throughout, we consider second order centered finite difference discretizations for all occurring derivatives. The Explicit Jump Immersed Interface Method is used to treat irregular boundaries. For details of this discretization of an elliptic equation we refer the reader to [35].

We embed  $\Omega$  so that its closure is contained in the rectangle  $R$ , and extend  $u$  and  $v$  by zero on the open complement of  $\Omega$  in  $R$ ,  $R \setminus \text{cl}\{\Omega\}$ . We will denote this open complement by  $\Omega^+$ , and write  $\Omega^-$  for the original domain  $\Omega$ . The extended functions  $u$  and  $v$  are in general discontinuous across  $\partial\Omega$ , with non-trivial jumps in all derivatives that are determined by the boundary conditions and derived below. If  $q$  is a function on  $R$  and  $\alpha$  is a point on  $\partial\Omega^-$ , the jump of  $q$  at  $\alpha$  is

$$[q](\alpha) = \lim_{x^+ \rightarrow \alpha} \lim_{\text{in } \Omega^+} q(x^+) - \lim_{x^- \rightarrow \alpha} \lim_{\text{in } \Omega^-} q(x^-).$$

The Explicit Jump Immersed Interface Method requires a complete set of independent jump conditions for all variables and their derivatives in the coordinate directions below the order of the discretization to achieve the same convergence rate that is obtained on rectangles.

**4.1. Displacement boundary conditions.** The jumps in displacements do not involve the differential geometry of the boundary, and can be written out immediately for Cartesian coordinates.

An extension of  $u$  and  $v$  by zero on  $R \setminus \text{cl}\{\Omega\}$ , where  $R = [a, b] \times [c, d]$ , and defining

$$\begin{aligned} \tilde{f}^u &= \begin{cases} -f^u/(\mu + \lambda) & \text{in } \Omega \\ 0 & \text{in } R \setminus \text{cl}\{\Omega\} \end{cases} \\ \tilde{f}^v &= \begin{cases} -f^v/(\mu + \lambda) & \text{in } \Omega \\ 0 & \text{in } R \setminus \text{cl}\{\Omega\} \end{cases} \end{aligned}$$

yields the differential equation on the rectangle  $R$  that the Explicit Jump Immersed Interface Method works on:

$$C\Delta u + u_{xx} + v_{xy} = \tilde{f}^u \text{ in } R \setminus \partial\Omega,$$

$$C\Delta v + u_{xy} + v_{yy} = \tilde{f}^v \text{ in } R \setminus \partial\Omega$$

with boundary conditions

$$v_x = u = 0 \text{ on } \Gamma_3 = \{x \in [a, b], y \in [c, d]\} \subset \partial R, \quad (5)$$

$$u_x = v = 0 \text{ on } \Gamma_3 = \{y \in [c, d], x \in [a, b]\} \subset \partial R. \quad (6)$$

The fact that  $u$  and  $v$  satisfy the same equation in  $\Omega^+$  as in  $\Omega^-$  and the choice of these particular “normal” boundary conditions on  $\partial R$  is essential for the use of a fast solver on  $R$ .

Across  $\Gamma_1$ , the jump conditions are

$$[u] = -\bar{u} \text{ on } \Gamma_1, \quad (7)$$

$$[v] = -\bar{v} \text{ on } \Gamma_1, \quad (8)$$

$$\left[ \frac{\partial^m u}{\partial x^i \partial y^{(m-i)}} \right] = -\frac{\partial^m u^-}{\partial x^i \partial y^{(m-i)}}, \quad i = 0, 1, \dots, m; \quad m = 1, 2, \dots \quad (9)$$

$$\left[ \frac{\partial^m v}{\partial x^i \partial y^{(m-i)}} \right] = -\frac{\partial^m v^-}{\partial x^i \partial y^{(m-i)}}, \quad i = 0, 1, \dots, m; \quad m = 1, 2, \dots \quad (10)$$

Alternatively, the equation and approximations of tangential derivatives may be used to derive jump conditions for second and higher derivatives as suggested in [35] and previously in [15].

**Theorem 1.** *When  $\Gamma_1 = \partial\Omega$ , the extension of  $u$  and  $v$  by zero is the unique solution of the extended problem on  $R$ , where  $u$  and  $v$  satisfy normal boundary conditions (5)–(6) on  $\partial R$ , the elastostatic equations (1)–(2) in  $\Omega^-$  and in  $\Omega^+$ , and the jump conditions (7)–(10). In other words, the restriction to  $\Omega^-$  of the solution of the extended problem solves the original boundary value problem (1)–(3).*

*Proof.* By design, the extended functions  $u$  and  $v$  satisfy the boundary conditions on  $R$ , the jump conditions on  $\partial\Omega$  and the differential equations in  $\Omega^-$  and  $\Omega^+$ . If any  $u$  and  $v$  satisfy (9)–(10), this implies  $u_x^+ = u_y^+ = v_x^+ = v_y^+ = \dots = v_{yy}^+ = 0$ . This, together with the facts that  $u$  and  $v$  satisfy (5)–(6) on  $\partial R$  and satisfy the elastostatic equations in  $\Omega^+$  guarantee that  $u$  and  $v$  vanish on  $\Omega^+$ . But then  $u^+ = v^+ = 0$ . Together with this, (7) and (8) imply that  $u^- = \bar{u}$  and  $v^- = \bar{v}$ . But then the uniqueness of  $u$  and  $v$  on  $\Omega^-$  is exactly the assumed uniqueness of the solution of the original boundary value problem.  $\square$

**4.2. Traction boundary conditions.** Different from displacement boundary conditions, traction boundary conditions are more conveniently expressed in the local coordinates of the boundary, i.e. derivatives in the tangent and normal directions. The traction boundary condition couples the two Cartesian displacement variables.

**4.2.1. Jumps in local coordinates.** Again the goal in this section is to get a complete set of jump conditions from the traction boundary conditions upon extending the solution by zero.

For concreteness, we may think of (4) as realized in Cartesian coordinates. Then  $\mathbf{u} = (u, v)$  is the vector of displacements in the  $x$ - and  $y$ - directions,  $\boldsymbol{\sigma}$  is the stress tensor expressed in  $(x, y)$  coordinates,  $\mathbf{n} = (n_1, n_2)$  is the inward normal to the boundary (given in  $(x, y)$  coordinates) and  $\mathbf{g}$  is a vector of surface forces applied at that boundary, also given in  $(x, y)$  coordinates.

We indicate the tangent to the boundary by  $\mathbf{t} = (n_2, -n_1)$  so that  $(\mathbf{t}, \mathbf{n})$  form a right hand system. The displacements in this coordinate system are  $\xi = \mathbf{u} \cdot \mathbf{n}$  and  $\eta = \mathbf{u} \cdot \mathbf{t}$ . We



think of gradients as row vectors, so  $\nabla \mathbf{u} = \begin{pmatrix} u_x & u_y \\ v_x & v_y \end{pmatrix}$ , and use the notation

$$\xi_n = \nabla (\mathbf{u} \cdot \mathbf{n}) \mathbf{n} = \mathbf{n}^T (\nabla \mathbf{u}) \mathbf{n}, \quad (11)$$

$$\eta_n = \nabla (\mathbf{u} \cdot \mathbf{t}) \mathbf{n} = \mathbf{n}^T (\nabla \mathbf{u}) \mathbf{t}, \quad (12)$$

$$\xi_t = \nabla (\mathbf{u} \cdot \mathbf{n}) \mathbf{t} = \mathbf{t}^T (\nabla \mathbf{u}) \mathbf{n}, \quad (13)$$

$$\eta_t = \nabla (\mathbf{u} \cdot \mathbf{t}) \mathbf{t} = \mathbf{t}^T (\nabla \mathbf{u}) \mathbf{t}. \quad (14)$$

We rewrite (4) in these *local coordinates* that are implied by the geometry of the boundary and change with the boundary

$$\left( \frac{E}{2(1+\nu)} \begin{pmatrix} 2\xi_n & \xi_t + \eta_n \\ \xi_t + \eta_n & 2\eta_t \end{pmatrix} + \frac{E\nu}{(1+\nu)(1-2\nu)} \begin{pmatrix} \xi_n + \eta_t & 0 \\ 0 & \xi_n + \eta_t \end{pmatrix} \right) \begin{pmatrix} 1 \\ 0 \end{pmatrix} = \begin{pmatrix} \mathbf{g} \cdot \mathbf{n} \\ \mathbf{g} \cdot \mathbf{t} \end{pmatrix}.$$

From this we derive formulas for the normal derivatives of the displacements in terms of tangential derivatives.

$$\xi_n = -\tilde{g}^\xi - \frac{\nu}{1-\nu} \eta_t, \quad (15)$$

$$\eta_n = -\tilde{g}^\eta - \xi_t, \quad (16)$$

where

$$\tilde{g}^\xi = -\frac{(1+\nu)(1-2\nu)\mathbf{g} \cdot \mathbf{n}}{E(1-\nu)},$$

$$\tilde{g}^\eta = -\frac{2(1+\nu)\mathbf{g} \cdot \mathbf{t}}{E}.$$

Now we have a complete set of jump conditions, albeit some not yet in Cartesian coordinates.

$$[\mathbf{u}] = -\mathbf{u}^- \text{ on } \Gamma_2, \quad (17)$$

$$[v] = -v^- \text{ on } \Gamma_2, \quad (18)$$

$$[\xi_n] = -\xi_n^- = \tilde{g}^\xi + \frac{\nu}{1-\nu} \eta_t^- \text{ on } \Gamma_2, \quad (19)$$

$$[\eta_n] = -\eta_n^- = \tilde{g}^\eta + \xi_t^- \text{ on } \Gamma_2, \quad (20)$$

$$[\xi_t] = -\xi_t^- \text{ on } \Gamma_2, \quad (21)$$

$$[\eta_t] = -\eta_t^- \text{ on } \Gamma_2. \quad (22)$$

The second and higher order jumps  $[u_{xx}]$ ,  $[u_{xy}]$ ,  $\dots$ ,  $[v_{yyy}]$  are the same as in the displacement case, (9)—(10) for  $m \geq 2$ . The derivations in §4.2.2 bring (19)—(22) into the form required by the Explicit Jump Immersed Interface Method.

**4.2.2. Jumps in Cartesian coordinates.** Equations (11)—(14) can be used for coordinate transformations of jumps:

$$\begin{pmatrix} \mathbf{n}^T \\ \mathbf{t}^T \end{pmatrix} \begin{pmatrix} [u_x] & [u_y] \\ [v_x] & [v_y] \end{pmatrix} \begin{pmatrix} \mathbf{n} & \mathbf{t} \end{pmatrix} = \begin{pmatrix} [\xi_n] & [\eta_n] \\ [\xi_t] & [\eta_t] \end{pmatrix}$$

or, using the orthonormality of  $(\mathbf{n}, \mathbf{t})$ ,

$$\begin{pmatrix} [u_x] & [u_y] \\ [v_x] & [v_y] \end{pmatrix} = \begin{pmatrix} \mathbf{n} & \mathbf{t} \end{pmatrix} \begin{pmatrix} [\xi_n] & [\eta_n] \\ [\xi_t] & [\eta_t] \end{pmatrix} \begin{pmatrix} \mathbf{n}^T \\ \mathbf{t}^T \end{pmatrix}.$$

Observe that

$$\begin{pmatrix} [\xi_n] & [\eta_n] \\ [\xi_t] & [\eta_t] \end{pmatrix} = \begin{pmatrix} \tilde{g}^\xi & \tilde{g}^\eta \\ 0 & 0 \end{pmatrix} + \begin{pmatrix} \frac{\nu}{1-\nu} \eta_t^- & \xi_t^- \\ -\xi_t^- & -\eta_t^- \end{pmatrix}$$

and get

$$\begin{aligned} [u_x] &= (n_1 \quad t_1) \left( \begin{pmatrix} \tilde{g}^\xi & \tilde{g}^\eta \\ 0 & 0 \end{pmatrix} + \begin{pmatrix} \frac{\nu}{1-\nu} \eta_t^- & \xi_t^- \\ -\xi_t^- & -\eta_t^- \end{pmatrix} \right) \begin{pmatrix} n_1 \\ t_1 \end{pmatrix}, \\ [u_y] &= (n_1 \quad t_1) \left( \begin{pmatrix} \tilde{g}^\xi & \tilde{g}^\eta \\ 0 & 0 \end{pmatrix} + \begin{pmatrix} \frac{\nu}{1-\nu} \eta_t^- & \xi_t^- \\ -\xi_t^- & -\eta_t^- \end{pmatrix} \right) \begin{pmatrix} n_2 \\ t_2 \end{pmatrix}, \\ [v_x] &= (n_2 \quad t_2) \left( \begin{pmatrix} \tilde{g}^\xi & \tilde{g}^\eta \\ 0 & 0 \end{pmatrix} + \begin{pmatrix} \frac{\nu}{1-\nu} \eta_t^- & \xi_t^- \\ -\xi_t^- & -\eta_t^- \end{pmatrix} \right) \begin{pmatrix} n_1 \\ t_1 \end{pmatrix}, \\ [v_y] &= (n_2 \quad t_2) \left( \begin{pmatrix} \tilde{g}^\xi & \tilde{g}^\eta \\ 0 & 0 \end{pmatrix} + \begin{pmatrix} \frac{\nu}{1-\nu} \eta_t^- & \xi_t^- \\ -\xi_t^- & -\eta_t^- \end{pmatrix} \right) \begin{pmatrix} n_2 \\ t_2 \end{pmatrix}. \end{aligned}$$

Putting it all together,

$$\begin{aligned} [u_x] &= \left( \frac{\nu}{1-\nu} n_1^2 - t_1^2 \right) \eta_t^- + n_1^2 \tilde{g}^\xi + n_1 t_1 \tilde{g}^\eta, \\ [u_y] &= \left( \frac{\nu}{1-\nu} n_1 n_2 - t_1 t_2 \right) \eta_t^- + (n_1 t_2 - n_2 t_1) \xi_t^- + n_1 n_2 \tilde{g}^\xi + n_1 t_2 \tilde{g}^\eta, \\ [v_x] &= \left( \frac{\nu}{1-\nu} n_2 n_1 - t_2 t_1 \right) \eta_t^- + (n_2 t_1 - t_2 n_1) \xi_t^- + n_2 n_1 \tilde{g}^\xi + n_2 t_1 \tilde{g}^\eta, \\ [v_y] &= \left( \frac{\nu}{1-\nu} n_2^2 - t_2^2 \right) \eta_t^- + n_2^2 \tilde{g}^\xi + n_2 t_2 \tilde{g}^\eta, \end{aligned}$$

where

$$\begin{aligned} \eta_t^- &= (t_1, t_2) \begin{pmatrix} u_x^- & u_y^- \\ v_x^- & v_y^- \end{pmatrix} \begin{pmatrix} t_1 \\ t_2 \end{pmatrix} = t_1^2 u_x^- + t_1 t_2 u_y^- + t_2 t_1 v_x^- + t_2^2 v_y^-, \\ \xi_t^- &= (t_1, t_2) \begin{pmatrix} u_x^- & u_y^- \\ v_x^- & v_y^- \end{pmatrix} \begin{pmatrix} n_1 \\ n_2 \end{pmatrix} = t_1 n_1 u_x^- + t_1 n_2 u_y^- + t_2 n_1 v_x^- + t_2 n_2 v_y^-. \end{aligned}$$

**4.3. Weighted Least Squares grid-to-interface extrapolation of function and derivative values.** The least squares fit idea was used to second order in [15] for interfaces in order to improve the stability for the Immersed Interface Method in the presence of large jumps in the coefficient. Here, we describe it to third order and in the one-sided limit context of the Explicit Jump Immersed Interface Method. It is a general method to impose boundary conditions and jump conditions on non-grid-aligned boundaries and interfaces that is easily programmed and easily extended to three space dimensions.

*4.3.1. Third order weighted least squares fit.* Figure 3 shows an annulus embedded in a square. The annulus is not centered in the square in order to avoid symmetry in the grid effects in later considerations. The heavy dot marks an intersection of a boundary with the mesh and the circles mark grid points inside the domain within distance  $r$  from the boundary point that are used to extrapolate function and derivative values from the grid to the boundary. The arrow points in the outward normal direction to the boundary, denoted by  $\mathbf{n} = (c, s)$ . We denote the coordinates of the boundary-mesh intersection by  $(x_\alpha, y_\alpha)$  and a generic marked grid point by  $(x_i, y_j)$ . Let  $h_i = x_i - x_\alpha$  and  $k_j = y_j - y_\alpha$ . The restriction  $R$  selects the values  $U_R$  of a grid function  $U$  at the marked grid points. The bi-cubic polynomial  $p$  should ideally satisfy  $u_{ij} = p(x_i, y_j)$ , where  $p(x_i, y_j) = p_0 + p_1 h_i + p_2 k_j + p_3 h_i^2 + p_4 h_i k_j + p_5 k_j^2 + p_6 h_i^3 + p_7 h_i^2 k_j + p_8 h_i k_j^2 + p_9 k_j^3$ , for each of the marked grid points. We will discuss this interpolation in more detail in §4.3.2. On  $n_l > 10$  grid points, this linear system is overdetermined. We use a least squares fit and introduce weights that allow better approximation closer to the extrapolation point. For example, one could use  $w_{ij} = (1 + \cos(\pi d_{ij}/r))/2$  as in [15], where  $0 \leq d_{ij} = \sqrt{h_i^2 + k_j^2} \leq r$ , and  $r$  is the ‘‘radius of influence’’. For these weights, due to the use of one-sided stencils, we found that we need to use larger  $r$  than does Li in [15]. To be able to use a smaller radius of influence  $r$ , we adjusted the weights,  $w_{ij} = 1/(1 + d_{ij}/h)$ .

The weighted least squares problem for the coefficients of  $p$  is then

$$\min_p \sum_{l=1}^{n_l} w_{ij(l)}^2 (p(x_{i(l)}, y_{j(l)}) - u_{ij(l)})^2,$$

where  $n_l$  is the number of marked points and the minimum is taken over all bi-cubic polynomials  $p$ . Letting<sup>1</sup>  $W = \text{diag}((w_{ij(l)})_{l=1}^{n_l})$ ,  $P = [p_0, p_1, \dots, p_9]^T$  and using the  $n_l \times 10$  matrix  $M$  with rows corresponding to grid points, i.e.  $l^{\text{th}}$  row

$$M_l = [1, h_{i(l)}, k_{j(l)}, h_{i(l)}^2, h_{i(l)} k_{j(l)}, k_{j(l)}^2, h_{i(l)}^3, h_{i(l)}^2 k_{j(l)}, h_{i(l)} k_{j(l)}^2, k_{j(l)}^3],$$

we find that for a given grid function  $U$ , the coefficients of the weighted least squares fit polynomial are given by  $P = (M^T W^2 M)^{-1} M^T W^2 R U$ . In the Explicit Jump Immersed Interface framework, the grid function  $U$  is not known but has to satisfy jump conditions. These can be expressed conveniently using rows of the matrix  $D = S(M^T W^2 M)^{-1} M^T W^2 R$ , where  $S = \text{diag}(1, 1, 1, 2, 1, 2, 1, 2, 6, 2, 2, 6)$ . This is true because  $p$  was derived with origin  $(x_\alpha, y_\alpha)$ , so function values and derivative values of  $U$  at the boundary point are approximated as follows:

$$\begin{aligned} u(x_\alpha, y_\alpha) &= p_0 + \mathcal{O}(h^4), \\ u_x(x_\alpha, y_\alpha) &= p_1 + \mathcal{O}(h^3), \\ u_y(x_\alpha, y_\alpha) &= p_2 + \mathcal{O}(h^3), \\ u_{xx}(x_\alpha, y_\alpha) &= 2p_3 + \mathcal{O}(h^2), \\ u_{xy}(x_\alpha, y_\alpha) &= p_4 + \mathcal{O}(h^2), \\ u_{yy}(x_\alpha, y_\alpha) &= 2p_5 + \mathcal{O}(h^2), \\ u_{xxx}(x_\alpha, y_\alpha) &= 6p_6 + \mathcal{O}(h), \\ u_{xxy}(x_\alpha, y_\alpha) &= 2p_7 + \mathcal{O}(h), \\ u_{xyy}(x_\alpha, y_\alpha) &= 2p_8 + \mathcal{O}(h), \\ u_{yyy}(x_\alpha, y_\alpha) &= 6p_9 + \mathcal{O}(h). \end{aligned}$$

For example, a condition on the directional derivative normal to the boundary can be written in terms of  $cD_2 + sD_3$ , where  $(c, s)$  is the unit normal and  $D_2$  and  $D_3$  are the second and third rows of  $D$ , respectively, which correspond to taking the  $x$  and  $y$  derivatives of  $U$  at  $(x_\alpha, y_\alpha)$ .

**4.3.2. Remarks on interpolation.** Lorentz [16] discusses analytic conditions under which quadratic interpolation on six points in 2D is possible; this is used in [35]. Similar limitations hold for third order interpolation on 10 points. We found it easiest to deal with this issue numerically, independently of the number of points in the stencil. Whenever  $M^T W^2 M$  is singular or close to singular, we know that the geometry results in a bad stencil and revert to a second order weighted least squares fit. If that fails also, we revert to first order. Since derivatives are needed to enforce traction boundary conditions, first order is the minimum that we need to be able to use. If  $M^T W^2 M$  is singular even in that case, then a finer mesh is needed to resolve the geometry.

**4.4. Corrections for Laplacian and cross derivatives to  $\mathcal{O}(h^2)$ .** Consider the situation of an interface  $\Gamma$  in the neighborhood of the point  $(x_i, y_j)$  as seen in Figure 4. Similar to Peskin's (first order) Immersed Boundary Method, we consider the discontinuity along an interface as being "spread onto a grid". The difference is that we are guided by "sharpness", i.e. achieve the smallest possible influence stencil, and want to achieve the

<sup>1</sup>The notation  $\text{diag}(\text{vector})$  indicates a square diagonal matrix with the vector on the diagonal.

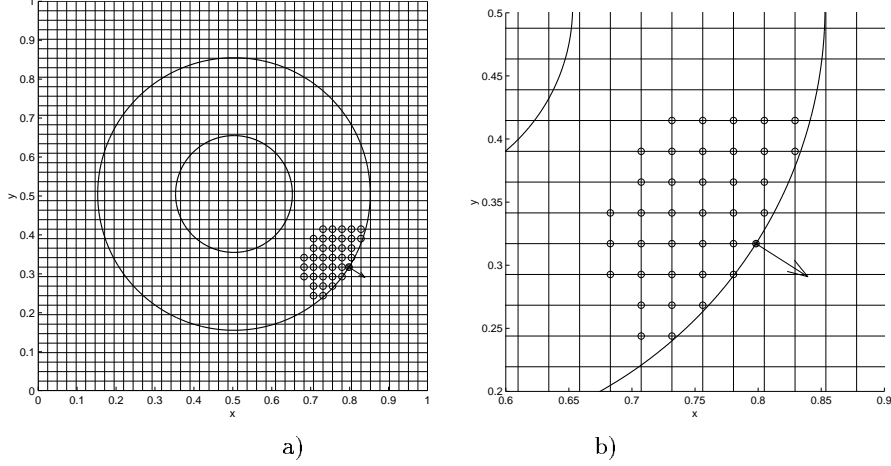


FIGURE 3. In a), we see an annulus embedded in a square. b) shows a blowup of the same figure. The heavy dot marks an intersection of the annulus boundary with the mesh, the circles mark grid points inside the domain within distance  $r$  from the boundary point. The arrow points in the outward normal direction to the boundary.

highest possible order of the truncation error — here  $\mathcal{O}(h^2)$  for all terms that need to be discretized in 2D linear elastostatics, extending the derivations in [35] which were  $\mathcal{O}(h)$ .

4.4.1. *The Laplacian.* As in [35], discontinuities along  $\Gamma$ , imposed at  $\alpha_1, \alpha_2, \alpha_3, \alpha_4$  and  $\alpha_5$  lead to the following corrections for the Laplacian at  $(x_i, y_j)$ :

$$\begin{aligned} \Delta u(x_i, y_j) &= \frac{u(x_{i+1}, y_j) + u(x_{i-1}, y_j) + u(x_i, y_{j+1}) + u(x_i, y_{j-1}) - 4u(x_i, y_j)}{h^2} \\ &\quad - \frac{1}{h^2} \sum_{m=0}^3 \frac{(h_3^+)^m}{m!} \left[ \frac{\partial^m u}{\partial x^m} \right]_{\alpha_3} - \frac{1}{h^2} \sum_{m=0}^3 \frac{(k_4^+)^m}{m!} \left[ \frac{\partial^m u}{\partial y^m} \right]_{\alpha_4} \\ &\quad - \frac{1}{h^2} \sum_{m=0}^3 \frac{(k_2^+)^m}{m!} \left[ \frac{\partial^m u}{\partial y^m} \right]_{\alpha_2} + \mathcal{O}(h^2). \end{aligned}$$

The only other grid point where the jumps at  $\alpha_3$  enter the discretization of the Laplacian is the second neighboring grid point,  $(x_{i+1}, y_j)$ :

$$\begin{aligned} \Delta u(x_{i+1}, y_j) &= \frac{u(x_{i+2}, y_j) + u(x_i, y_j) + u(x_{i+1}, y_{j+1}) + u(x_{i+1}, y_{j-1}) - 4u(x_{i+1}, y_j)}{h^2} \\ &\quad - \frac{1}{h^2} \sum_{m=0}^3 \frac{(h_3^-)^m}{m!} \left[ \frac{\partial^m u}{\partial x^m} \right]_{\alpha_3} + \mathcal{O}(h^2). \end{aligned}$$

This is true in general: For the discretization of the Laplacian, every intersection of interface and mesh only affects its nearest two grid neighbors.

4.4.2. *Cross derivatives.* For the discretization of  $u_{xy} = \partial^2 / \partial x \partial y$ , think of

$$\begin{aligned} u_{xy}(x_i, y_j) &= \frac{1}{2} \frac{\frac{u(x_{i+1}, y_{j+1}) - u(x_{i-1}, y_{j+1})}{2h} - \frac{u(x_{i+1}, y_{j-1}) - u(x_{i-1}, y_{j-1})}{2h}}{2h} \\ &\quad + \frac{1}{2} \frac{\frac{u(x_{i+1}, y_{j+1}) - u(x_{i+1}, y_{j-1})}{2h} - \frac{u(x_{i-1}, y_{j+1}) - u(x_{i-1}, y_{j-1})}{2h}}{2h} + \mathcal{O}(h^2). \end{aligned} \quad (23)$$

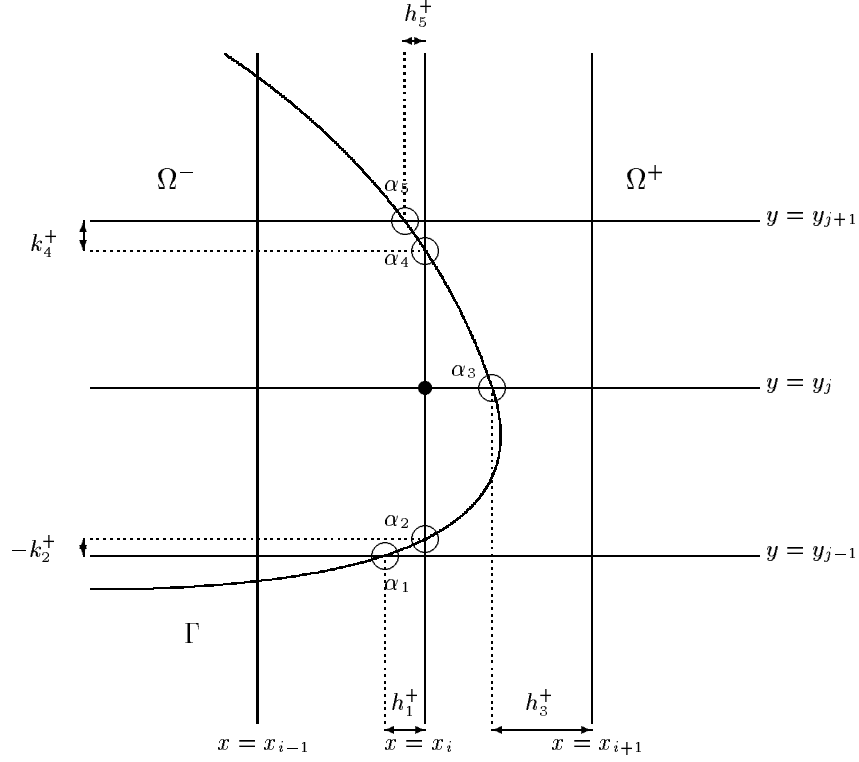


FIGURE 4. Interface and mesh geometry near a lattice point  $(x_i, y_j)$ . Five intersections of the interface and the mesh affect the discretization of linear elastostatics for the point  $(x_i, y_j)$ ; they are labeled  $\alpha_1, \alpha_2, \dots, \alpha_5$ .

In the case of smooth functions, we simply add the same terms, but in the presence of an interface, the difference approximations require different corrections. In the case illustrated in Figure 4 we break the corrections into pieces:

$$u_x(x_i, y_{j+1}) = \frac{u(x_{i+1}, y_{j+1}) - u(x_{i-1}, y_{j+1})}{2h} - \frac{1}{2h} \sum_{m=0}^3 \frac{(h_5^-)^m}{m!} \left[ \frac{\partial^m u}{\partial x^m} \right]_{\alpha_5} + \frac{2}{2h} \frac{h^3}{6} u_{xxx}(x_i, y_{j+1}) + \mathcal{O}(h^3)$$

and

$$u_x(x_i, y_{j-1}) = \frac{u(x_{i+1}, y_{j-1}) - u(x_{i-1}, y_{j-1})}{2h} - \frac{1}{2h} \sum_{m=0}^3 \frac{(h_1^-)^m}{m!} \left[ \frac{\partial^m u}{\partial x^m} \right]_{\alpha_1} + \frac{2}{2h} \frac{h^3}{6} u_{xxx}(x_i, y_{j-1}) + \mathcal{O}(h^3).$$

Also,

$$u_{xy}(x_i, y_j) = \frac{u_x(x_i, y_{j+1}) - u_x(x_i, y_{j-1})}{2h} - \frac{1}{2h} \sum_{m=0}^2 \frac{(k_4^+)^m}{m!} \left[ \frac{\partial^{m+1} u}{\partial x \partial y^m} \right]_{\alpha_4} - \frac{1}{2h} \sum_{m=0}^2 \frac{(k_2^+)^m}{m!} \left[ \frac{\partial^{m+1} u}{\partial x \partial y^m} \right]_{\alpha_2} + \mathcal{O}(h^2).$$

Hence

$$\begin{aligned}
u_{xy}(x_i, y_j) &= \frac{u(x_{i+1}, y_{j+1}) - u(x_{i-1}, y_{j+1})}{4h^2} - \frac{u(x_{i-1}, y_{j+1}) - u(x_{i-1}, y_{j-1})}{4h^2} \\
&\quad - \frac{1}{2h} \sum_{m=0}^2 \frac{(k_4^+)^m}{m!} \left[ \frac{\partial^{m+1} u}{\partial x \partial y^m} \right]_{\alpha_4} - \frac{1}{2h} \sum_{m=0}^2 \frac{(k_2^+)^m}{m!} \left[ \frac{\partial^{m+1} u}{\partial x \partial y^m} \right]_{\alpha_2} \\
&\quad - \frac{1}{4h^2} \sum_{m=0}^3 \frac{(h_1^-)^m}{m!} \left[ \frac{\partial^m u}{\partial x^m} \right]_{\alpha_1} - \frac{1}{4h^2} \sum_{m=0}^3 \frac{(h_5^-)^m}{m!} \left[ \frac{\partial^m u}{\partial x^m} \right]_{\alpha_5} \\
&\quad + \frac{h}{12} u_{xxx}(x_i, y_{j+1}) - \frac{h}{12} u_{xxx}(x_i, y_{j-1}) + \mathcal{O}(h^2).
\end{aligned}$$

Now use  $u_{xxx}(x_i, y_{j+1}) = u_{xxx}(x_i, y_j) + [u_{xxx}]_{\alpha_4} + \mathcal{O}(h)$  and  $u_{xxx}(x_i, y_{j-1}) = u_{xxx}(x_i, y_j) + [u_{xxx}]_{\alpha_2} + \mathcal{O}(h)$  and get

$$\begin{aligned}
u_{xy}(x_i, y_j) &= \frac{u(x_{i+1}, y_{j+1}) - u(x_{i-1}, y_{j+1})}{4h^2} - \frac{u(x_{i+1}, y_{j-1}) - u(x_{i-1}, y_{j-1})}{4h^2} \\
&\quad - \frac{1}{2h} \sum_{m=0}^2 \frac{(k_4^+)^m}{m!} \left[ \frac{\partial^{m+1} u}{\partial x \partial y^m} \right]_{\alpha_4} - \frac{1}{2h} \sum_{m=0}^2 \frac{(k_2^+)^m}{m!} \left[ \frac{\partial^{m+1} u}{\partial x \partial y^m} \right]_{\alpha_2} \\
&\quad - \frac{1}{4h^2} \sum_{m=0}^3 \frac{(h_1^-)^m}{m!} \left[ \frac{\partial^m u}{\partial x^m} \right]_{\alpha_1} - \frac{1}{4h^2} \sum_{m=3}^2 \frac{(h_5^-)^m}{m!} \left[ \frac{\partial^m u}{\partial x^m} \right]_{\alpha_5} \\
&\quad + \frac{h}{12} \left[ \frac{\partial^3 u}{\partial x^3} \right]_{\alpha_4} - \frac{h}{12} \left[ \frac{\partial^3 u}{\partial x^3} \right]_{\alpha_2} + \mathcal{O}(h^2).
\end{aligned}$$

For the second term in (23), we find in a similar fashion

$$\begin{aligned}
u_{xy}(x_i, y_j) &= \frac{u(x_{i+1}, y_{j+1}) - u(x_{i+1}, y_{j-1})}{4h^2} - \frac{u(x_{i-1}, y_{j+1}) - u(x_{i-1}, y_{j-1})}{4h^2} \\
&\quad - \frac{1}{2h} \sum_{m=0}^2 \frac{(h_3^+)^m}{m!} \left[ \frac{\partial^{m+1} u}{\partial y \partial x^m} \right]_{\alpha_3} + \frac{h}{12} \left[ \frac{\partial^3 u}{\partial x^3} \right]_{\alpha_3} + \mathcal{O}(h^2).
\end{aligned}$$

Comparing with (23), intersection  $\alpha_1$  affects the second inner difference in the first term,  $\alpha_2$  affects the outer difference in the first term,  $\alpha_3$  affects the outer difference in the second term,  $\alpha_4$  affects the outer difference in the first term and  $\alpha_5$  affects the first inner difference in the first term.

Averaging terms in (23) has the effect of not giving preference to either the  $x$ - or  $y$ -direction, and allows a uniform treatment for all intersections. Every intersection always affects six grid points. The relative geometry of the six points depends only on whether the intersection occurs for a horizontal or vertical mesh line. The corrections are needed in four “inner differences” and two “outer differences”. The horizontal and vertical case each split up into two cases, depending which of the nearest grid neighbors of the intersection lies in  $\Omega^+$ . For example, interface-grid intersection  $\alpha_3$  affects the discretization of  $\partial^2/\partial x \partial y$  at the points  $(x_{i+1}, y_{j-1})$ ,  $(x_{i+1}, y_j)$ ,  $(x_{i+1}, y_{j+1})$ ,  $(x_i, y_{j-1})$ ,  $(x_i, y_j)$  and  $(x_i, y_{j+1})$ , and intersection  $\alpha_4$  affects the discretization of  $\partial^2/\partial x \partial y$  at the points  $(x_{i-1}, y_j)$ ,  $(x_{i-1}, y_{j+1})$ ,  $(x_i, y_j)$ ,  $(x_i, y_{j+1})$ ,  $(x_{i+1}, y_j)$  and  $(x_{i+1}, y_{j+1})$ .

*Remark 4.1.* In the case that an intersection coincides with a grid point, this point should be thought of as belonging to  $\Omega^-$  or  $\Omega^+$ , with intersections chosen accordingly.

*Remark 4.2.* Through our implementation we have found that the solutions may depend more smoothly on the geometry if we change the equations for exterior grid neighbors of the boundary from “corrected linear elastostatics” to “fix the value to zero”. To be able to use the fast solver from [33], this has to be implemented as a perturbation of the standard stencil as described in [35].

**4.5. Finding the displacements using an elastostatic solver.** Recall that boundary conditions on  $\partial\Omega$  are realized through jump conditions inside  $R$ . If the jumps were known, only the right hand side of the system of linear elastostatics on  $R$  would need to be modified, according to the formulas in §4.4. To take advantage of this fact the unknown jumps at the intersections of boundaries and mesh are introduced as auxiliary variables. The jump conditions (c.f. §4.1, §4.2) are discretized based on grid values of the displacements. For known grid functions  $\mathbf{U} = (U^T, V^T)^T$ , the jumps can be found simply by appropriately differencing the grid functions (c.f. §4.3). Symbolically, the system is thus

$$\begin{pmatrix} A & \Psi \\ D & I \end{pmatrix} \begin{pmatrix} \mathbf{U} \\ \mathbf{J} \end{pmatrix} = \begin{pmatrix} \mathbf{F}_1 \\ \mathbf{F}_2 \end{pmatrix}.$$

Here  $\mathbf{U}$  denotes the vector of stacked grid functions  $U$  and  $V$ ,  $\mathbf{J}$  is the vector of jumps,  $A$  is the matrix for the discretization of linear elastostatics by centered differences with normal boundary conditions, (5)—(6) on  $R$ ,  $\Psi$  is the matrix that distributes the jumps to the equations with appropriate coefficients (§4.4),  $D$  takes appropriate finite differences on the grid functions (§4.3, §4.1, §4.2) and  $I$  is an appropriately sized identity matrix. The first row in the above system discretizes the differential equation on  $R$ , the second row is the discretization of the jump conditions. Given jumps correspond to zero rows in  $D$  and non-zero entries in the right hand side  $\mathbf{F}_2$ .

Eliminating  $\mathbf{U}$  from the system using

$$\mathbf{U} = A^{-1} (\mathbf{F}_1 - \Psi\mathbf{J}), \quad (24)$$

we find a system for the jumps,

$$DA^{-1} (\mathbf{F}_1 - \Psi\mathbf{J}) + \mathbf{J} = \mathbf{F}_2,$$

that is

$$(I - DA^{-1}\Psi)\mathbf{J} = \mathbf{F}_2 - DA^{-1}\mathbf{F}_1. \quad (25)$$

This Schur-complement for the jumps is solved iteratively with GMRES ([22]) or BiCGSTAB ([31]), conjugate gradient methods for non-symmetric matrices. An iterative method is needed because  $A^{-1}$  is not known, but can be applied rapidly in  $\mathcal{O}(n \log n)$  using a fast elastostatic solver [33]. To make efficient use of the solver, the number of mesh points in each direction (after reflection, see [33]) should be a power of two. Once the jumps are known, the displacement vector  $\mathbf{U}$  is found applying the fast elastostatic solver one more time to evaluate (24).

*Remark 4.3.* This is the application of Schur-complement methods for Poisson problems on irregular domains from [35] (based on earlier work by Buzbee, Dorr, George and Golub[9] and the Capacitance matrix method by Proskurowski and Widlund [19], also used by Yang, [37]) to the elastostatic equations.

**4.6. The idea of the fast elastostatic solver.** The fast solver that applies  $A^{-1}$  in (25) requires  $\mathcal{O}(N \log N)$  operations to solve the elastostatic equations (1), (2) on a rectangle with normal boundary conditions, (5)—(6). It is based on the formulas for periodic boundary conditions. For  $c > 0$ ,  $1 \leq k \leq N_1$  and  $1 \leq m \leq N_2$ , but  $km > 1$

$$\bar{U}_{k,m} = \frac{d_{k,m}\bar{F}_{k,m}^u - b_{k,m}\bar{F}_{k,m}^v}{a_{k,m}d_{k,m} - b_{k,m}^2} h^2, \quad (26)$$

$$\bar{V}_{k,m} = \frac{a_{k,m}\bar{F}_{k,m}^v - b_{k,m}\bar{F}_{k,m}^u}{a_{k,m}d_{k,m} - b_{k,m}^2} h^2 \quad (27)$$

where  $N_1$  and  $N_2$  are the numbers of grid points in the horizontal and vertical directions, bars on capitalized variables indicate the two-dimensional Fourier transform and

$$\begin{aligned} a_{k,m} &= -4c - 2 + 2(c+1) \cos \frac{2\pi(k-1)}{N_1} + 2c \cos \frac{2\pi(m-1)}{N_2}, \\ b_{k,m} &= -\sin \frac{2\pi(k-1)}{N_1} \sin \frac{2\pi(m-1)}{N_2}, \\ d_{k,m} &= -4c - 2 + 2c \cos \frac{2\pi(k-1)}{N_1} + 2(c+1) \cos \frac{2\pi(m-1)}{N_2}. \end{aligned}$$

Due to the periodic boundary conditions we have to require that each component of the right hand side sums to zero, and after that the solution is unique only up to two constants. The problem with normal boundary conditions is solved using the solution for periodic boundary conditions on a larger problem that results from reflecting the right hand side as follows.

$f^u$	$f^v$	$-^u\lambda$	$^v\lambda$
$\lambda_{st}$	$-\lambda_{st}$	$-_nf$	${}_af$

This reflection naturally satisfies the condition that each component of the right hand side has to sum to zero. The undetermined constants arising from the solution of the periodic problem are both set to zero in order to match the displacement boundary conditions. Finally, the solution of the problem with normal boundary conditions is just the upper left block of the solution of the problem with periodic boundary conditions. A careful implementation [34] requires a sequence of one-dimensional FFTs on appropriately once-reflected (doubled) data structures and thus avoids the quadrupling described in [33].

For further details of the fast solver we refer to [33].



## 5. STRUCTURAL BOUNDARY DESIGN

So far, we have discussed techniques for computing the stresses given a particular design configuration. Our goal is to find the design that minimizes the total amount of material and keeps the compliance below a certain value, subject to loading and clamping boundary conditions. This is a constrained minimization problem; the constraint is the compliance, and the goal is to minimize the amount of material used in the design.

In many situations the solution of such a problem is not unique. An additional problem is that there may be many local minima: designs for which any small perturbation that satisfies the constraint require more material, yet the given shape is not the global minimum.

Our approach is an evolutionary one, see, for example, [36]. The principal idea is to remove material in regions of low stress and to add material in regions of high stress. We establish a removal rate  $RR$  which determines a percentage of the maximal initial stress below which material may be eliminated, and above which material should be added. The removal rate determines the closed stress contours along which new holes are cut and also the velocity of the boundary motion. It is increased only after no new holes are cut, and the design boundaries have stabilized. When the constraint is violated, the removal rate is decreased in order to add more material in regions of high stress and remove less material in regions of low stress. The lowered stresses are empirically seen to result also in lower values for the compliance. We terminate when this procedure cannot improve the weight while satisfying the compliance any more. Formally, we proceed as follows:

**Main Algorithm**

- 1: Initialize; find stresses in initial design.
- 2: While termination criteria are not satisfied do
- 3:   Cut new holes.
- 4:   Move boundaries.
- 5:   Find displacements, stresses, etc.
- 6:   If the constraints are violated reduce  $RR$  and revert to previous iteration.
- 7:   Update  $RR$ .

In order to execute this technique, we must accurately move the boundaries based on the stresses computed for the current design. It is important that this reconfiguration allow holes to merge, new holes to be cut, and the shape to continuously change topology under the trial motions. These requirements are handled well by level set methods, which we now briefly discuss. For more details, see [27, 28].

**5.1. Brief review of level set methods.** Level set methods were introduced by Osher and Sethian [18] and offer highly robust and accurate methods for tracking interfaces moving under complex motions. They grew out of the theory of curve and surface evolution developed by Sethian in [23, 24, 25], which constructs the notion of weak solutions and entropy limits for evolving interfaces, and links upwind numerical methodology for hyperbolic conservation laws to front propagation problems. The resulting level set approach works in any number of space dimensions, handles topological merging and breaking naturally, and is easy to program.

The level set method works by embedding the interface as the zero level set of a higher dimensional function. More precisely, given a moving closed hypersurface  $\Gamma(t)$ , that is,  $\Gamma(t=0) : [0, \infty) \rightarrow R^N$ , propagating with a speed  $F$  in its normal direction, we wish to produce an Eulerian formulation for the motion of the hypersurface propagating along its normal direction with speed  $F$ , where  $F$  can be a function of various arguments, including the curvature, normal direction, etc. Let  $\pm d$  be the signed distance to the interface. If we embed this propagating interface as the zero level set of a higher dimensional function  $\phi$ , that is, let  $\phi(x, t=0)$ , where  $x \in R^N$  is defined by

$$\phi(x, t=0) = \pm d, \tag{28}$$

then an initial value partial differential equation can be obtained for the evolution of  $\phi$ , namely

$$\phi_t + F|\nabla\phi| = 0 \quad (29)$$

$$\phi(x, t = 0) \text{ given} \quad (30)$$

This is known as the level set equation, introduced in [18] by Osher and Sethian. As discussed in [23, 24, 25], propagating fronts can develop shocks and rarefactions in the slope, corresponding to corners and fans in the evolving interface, and numerical techniques designed for hyperbolic conservation laws can be exploited to construct upwind schemes which produce the physically correct entropy solution.

The above formulation in fact reveals *two* central embeddings, each of which can be handled by computationally efficient algorithms.

5.1.1. *The Level Set Embedding.* First, in the initialization step (28), the signed distance function is used to build a function  $\phi$  which corresponds to the interface at the level set  $\phi = 0$ . This step is known as “initialization”; when performed at some later point in the calculation beyond  $t = 0$ , it is referred to as “re-initialization”. The need for re-initialization in level set methods was first discussed by Chopp in his work on minimal surfaces; see [11].

The algorithm for the level set equation (29) given in [18] uses upwind schemes based on an ENO-construction. As discussed in that paper, the level set equation is solved throughout the entire computational domain. This is impractical and inefficient. The algorithm becomes computationally efficient through the use of a *Narrow Band Level Set Method*, introduced by Adalsteinsson and Sethian [1], which confines computation to a narrow band around the interface of interest. The narrow band is of user-specified size. As the front moves and reaches the edge of the narrow band, the calculation is stopped, and a new initial level set function corresponding to the signed distance function is rebuilt. A very large narrow band means that one is essentially computing everywhere, and this re-initialization is never performed. A very thin narrow band means that one is computing only very close to the front, and hence re-initializing every time step. The numerical tests reported in [1] indicated that a narrow band of a particular size (around 6-10 grid points each side of the front) seems to be the correct balance between work spent updating points in the band, and work spent doing re-initialization.

5.1.2. *The Velocity Embedding.* Second, the construction of the initial value PDE given in (29) means that the velocity  $F$  is now defined for **all** the level sets, not just the zero level set corresponding to the interface itself. We can be more precise by rewriting the level set equation as

$$\phi_t + F_{ext}|\nabla\phi| = 0 \quad (31)$$

where  $F_{ext}$  is some velocity field which, at the zero level set, equals the given speed  $F$ . In other words,

$$F_{ext} = F \text{ on } \phi = 0$$

This new velocity field  $F_{ext}$  is known as the “extension velocity”.

In [2], Adalsteinsson and Sethian introduce a very fast technique for constructing this extension velocity, through the use of Fast Marching Methods [26], which are computational techniques for solving the Eikonal and related equations and rely on upwinding, causality principles, and heap sort techniques. The idea is as follows. Desirable properties of an extension velocity are that it should match the given velocity on the front itself, and that it should move the neighboring level sets in such a way that the signed distance function is preserved. Consider for a moment an initial signed distance function  $\phi(x, t = 0)$ , and suppose one builds an extension velocity of the form

$$\nabla F_{ext} \cdot \nabla\phi = 0, \quad (32)$$

as was discussed in [10]. It can be shown that the level set function  $\phi$  remains the signed distance function for all time, assuming that both  $F$  and  $\phi$  are smooth. Adalsteinsson and Sethian solve (32) in  $O(N \log N)$  time, where  $N$  is the total number of points where one wants to create this extension velocity. As such, it is a very efficient technique, and is warranted when a velocity is given only on an interface and must be extended throughout the narrow band in order to apply the level set update.

**5.2. Using the Narrow Band Level Set/Fast Marching Methods in structural boundary design.** By convention, the interior of the structure is labeled “negative”, the outside “positive”. In the narrow band, we maintain the distance from the structure boundaries, on the rest of the computational domain we keep track only of the sign of the distance function (in addition to the fact that we are outside of the narrow band). Several extensions of the basic narrow band level set method with extension velocities are required in structural boundary design.

*5.2.1. Cutting new holes.* A new hole is cut in the interior of the structure by computing its distance function in its own narrow band (with positive label inside the hole) and then taking the maximum of the two distance functions on the intersection of the narrow bands for the structure and the hole. On the non-intersecting parts of the narrow bands the distances are maintained. The union of the two narrow bands is the narrow band for the resulting structure.

*5.2.2. Hanging Nodes.* Hanging nodes occur when the boundary motion severs part of the structure from the non-trivial boundary conditions. Figure 5a) shows a domain with three holes that merge into one hole, Figure 5b). After the motion, two small islands of material are left inside the resulting hole.

In structural boundary design, subdomains that become disconnected from the nontrivial boundary conditions should be removed from the computations. Practically, they are not relevant and computationally, they become independent underdetermined subproblems. We detect and remove the disconnected component as follows. After the motion, we find the components of the zero contour of the distance function “from the outside toward the inside”, starting with the exterior boundary. From these, we rebuild a distance function. Hanging nodes are recognized as being cut into the “outside” portion of the structure based on the sign of the partially rebuilt distance function and ignored in the distance rebuilding phase.

*5.2.3. Stabilization of boundaries.* We do not cut new holes or change the removal rate for a few design steps after cutting one or more new holes, merging holes or after a change in the removal rate, because we observed that stress values immediately after these operations were not as reliable as under a stable boundary motion.

Another form of stabilization is symmetrization. For many of the problems in this paper, the structure geometry should remain symmetric due to the symmetry of the clamping and loading conditions. We found that unless we enforce this symmetry, ultimately round-off errors lead to the departure from this symmetry. Since in our cases the symmetry axis is usually aligned with a coordinate axis, we can simply symmetrize the geometry by averaging distance values on the sides of the symmetry axis.

*5.2.4. Velocities from stresses.* Recall that we solve for the displacements and difference them to find the (symmetric) stress tensor, with Lamé constants  $\mu$  and  $\lambda$ ,

$$\sigma = \mu \frac{\nabla \mathbf{u} + \nabla \mathbf{u}^T}{2} + \lambda \text{trace}(\nabla \mathbf{u}) I.$$

From the stress tensor, we calculate the von Mises stress as

$$S = \sqrt{\sigma_{11}^2 + \sigma_{22}^2 - \sigma_{11}\sigma_{22} + 3\sigma_{12}^2},$$

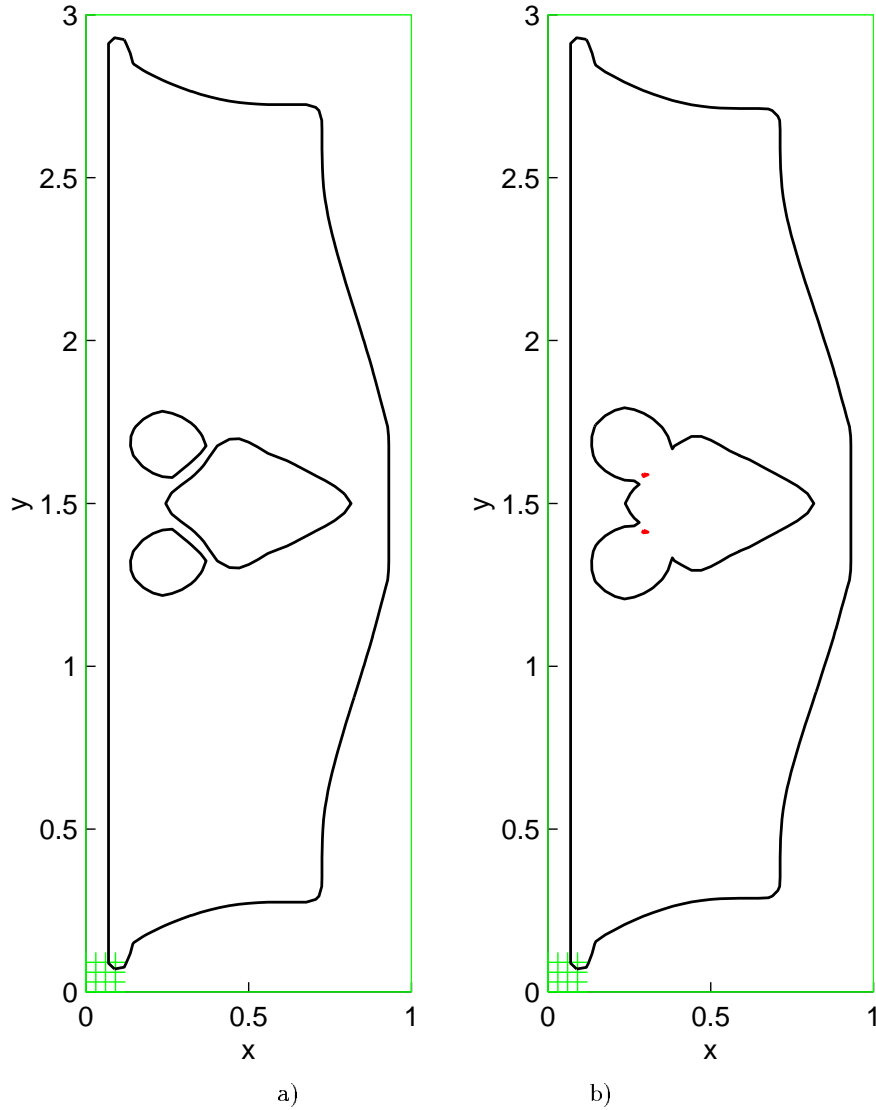


FIGURE 5. A domain with three holes a) that merge into one b). After the motion, two small islands of material are left inside the resulting hole. They have to be removed from the computations.

We extend the von Mises stress from the grid to the boundaries by the least squares extrapolation method from §4.3. In principle, for every component of the boundary the parameters of motion may be chosen separately, for example based on the maximal and minimal values of the stress on that component. In the examples in this paper, we distinguish only between the exterior boundary and hole boundaries. Five parameters describe the boundary motion.

1.  $s$ , a lower bound below which the boundary moves to reduce the structure with maximal speed.

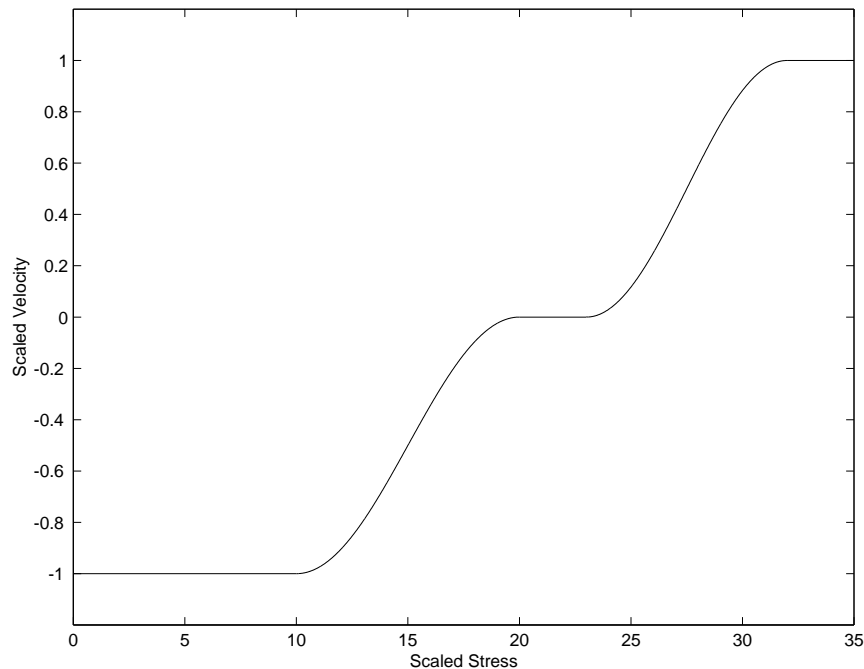


FIGURE 6. *The velocity profile for  $s = 10$ ,  $RR \approx \bar{s} = 20$ ,  $\bar{S} = 23$  and  $S = 32$ . The speed is at most one to allow for mesh-dependent scaling and automatic handling of a CFL condition in the level set motion.*

2.  $S$ , an upper bound below which the boundary moves to grow the structure with maximal speed.
3.  $\bar{s}$  and  $\bar{S}$  with  $s < \bar{s} < \bar{S} < S$  create an interval of stress values  $[\bar{s}, \bar{S}]$  in which the boundary does not move — an interval is needed to avoid shearing the boundary. By rescaling the intervals  $[s, \bar{s}]$  and  $[\bar{S}, S]$  to the interval  $[0, \pi]$  and using  $\pm(1 + \cos)/2$  on this interval we arrive at the  $C^1$  velocity profile depicted in Figure 6. This profile is scaled to have maximum absolute value  $2h/5$  to automatically satisfy a CFL condition.
4. The number of steps taken to advance the front. The velocity is chosen so that a single step is always allowable. To achieve similar motion on a differentd grid the number of steps has to be scaled inversely proportional to the change in mesh width.

5.2.5. *Velocity extension.* In the implementation, we extrapolate from grid points inside the structure to get stress values at the corners of a polygon whose corners results from calculating the intersections of the zero level set with the mesh lines of the level set mesh. From the stress values, we calculate the velocities at these points. All grid points inside the narrow band inherit the velocity from the nearest polygon point, with linear interpolation of velocities in the polygon segments. Figure 7 illustrates this procedure. At the corners, where the normal does not exist, the extension is different on the two sides of the polygon. On the side with the acute angle, the extension arrives from the interior of the polygon segments. On the side with the obtuse angle, there exists a region where the velocity is extended by the constant value from the corner point.

5.2.6. *Fixing boundaries.* The level set representation also allows inhibiting the motion of parts of the boundary. Following a suggestion by D. Adalsteinsson, we simply copy

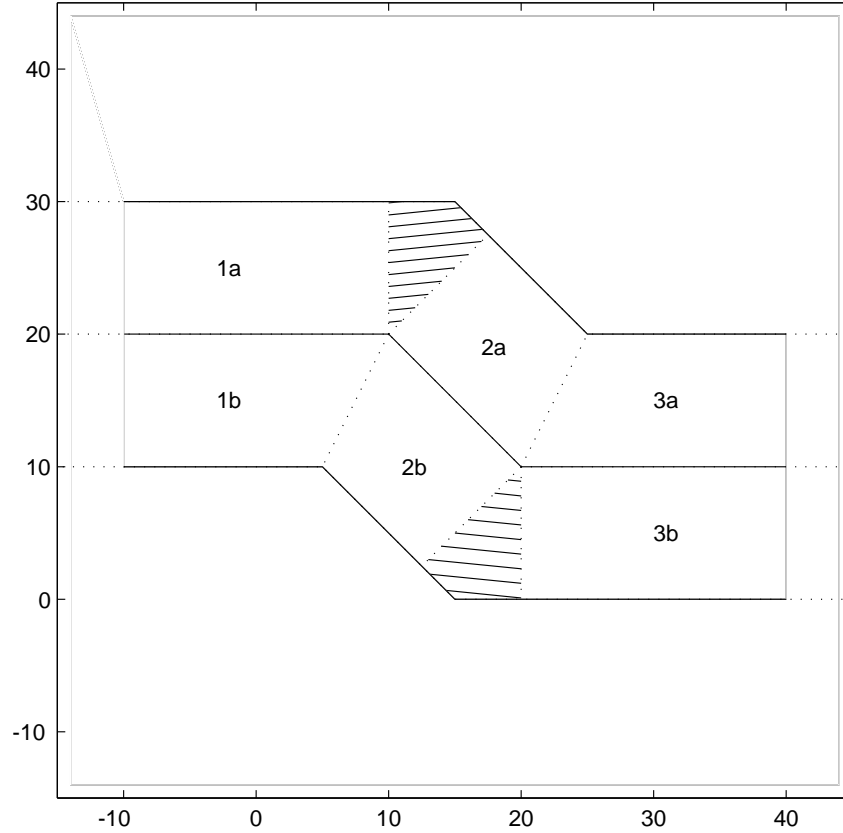


FIGURE 7. Values of velocity extension are only assigned inside the narrow band. In the shaded regions, the velocity is constant and equal to the value at the corner. In the other regions, the values are the same as on the nearest point in the polygon, where in turn the values are obtained by linear interpolation between the values at the corners.

values prior to the motion in regions that should not move. Similarly, it is possible to select only inward motion or outward motion on part of the domain by simple operations (e.g.  $\max(F, 0)$ , etc.) on the extended velocity on the grid.

**5.2.7. Choosing Parameter Values.** The final geometry found by our procedure depends on the choices of many parameters. This is typical for non-convex optimization problems and not unique to our approach. For example, it was observed also for the Reverse Adaptivity approach [20]. A typical value for the initial removal rate is between 0.01 and 0.1, the update is usually 0.01 or 0.025. The lower and upper bounds for the velocity typically are  $s = 0$ ,  $\bar{s} = RR$ ,  $\bar{S} = 1.1\bar{s}$  and  $S = \min(5.5\bar{s}, S_{\max})$ , where  $S_{\max}$  is the maximal stress in the initial design. The constraint on the compliance and on the maximal stress can be chosen arbitrarily. We terminate for example when a new design achieved under motion of  $RR = 0.01$  does not satisfy the constraint anymore.

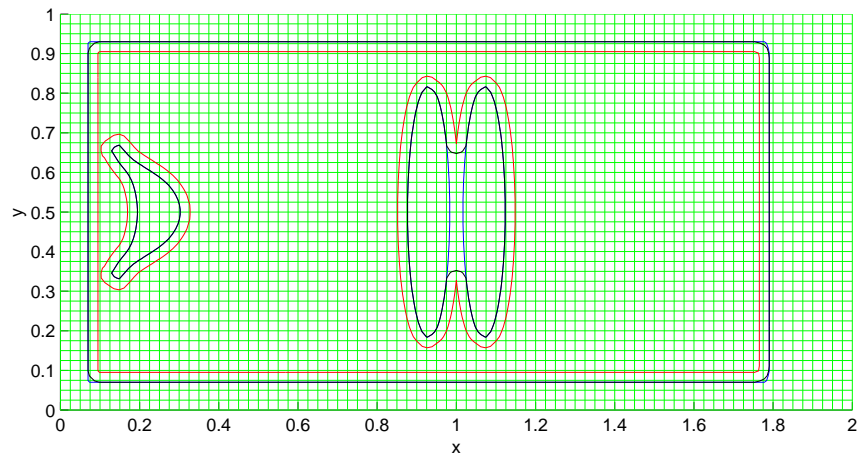


FIGURE 8. *Erosion and dilation remove the narrow truss between the two elongated ellipses, while all other boundary portions remain almost unchanged. The boundary motion is carried out on a different grid of half the shown meshwidth.*

### 5.3. Using the Immersed Interface Method in structural boundary design.

5.3.1. *Solving the pde when the structure gets “narrow”.* Geometries may arise in which the discretization to second order is not possible because there are not enough grid points inside the structure. This is the case especially for truss-like structures, where hole boundaries are close together and parallel over a length of three times the mesh size or more. To deal with these cases correctly, one could use a finer grid that resolves the geometry with enough grid points in the structure. But this is costly, especially when large parts of the domain are not yet truss-like. Alternatively, we can avoid the troublesome geometries using morphological operations suggested by A. Sarti. By eroding (shrinking) the structure by  $H$  and then dilating (growing) it by the same amount, we make sure that all trusses after this operation have width at least  $2H$ . To see this, note that in general, the structure changes very little under these operations. However, where a long, narrow truss of width less than  $2H$  was originally present, the erosion has removed it, and dilation cannot recreate it.

Figure 8 shows a rectangular cantilever with three holes on the computational grid. Erosion leads to the light gray boundaries, and dilation returns the boundaries to the original locations except for a little rounding of the corners and in the narrow region between the two ellipses that is too narrow for the discretization.

5.3.2. *Grid crossing.* For any fixed geometry, the Explicit Jump Immersed Interface Method converges with  $O(h^2)$ , but this says nothing about the quality of the solution when the grid is kept fixed and the boundary geometry is modified. In structural boundary design, whenever a boundary crosses a grid point, this point “enters” or “leaves” the structure and is newly used in the computation of the stresses or dropped from this computation. In this situation, the computed displacements and stresses may change discontinuously, even though the boundary motion is perfectly smooth. To improve this behavior, we abandoned the six point stencil approach from [32, 35] and use the weighted least squares from §4.3. This dramatically improves the “continuous” dependence of the computed stresses on the boundary shape.

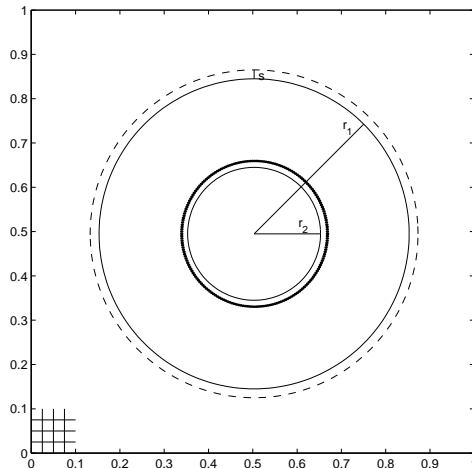


FIGURE 9. The annulus  $0.15 = r_2 < r < r_1 = 0.35$ , centered at  $(0.503, 0.495)$ . The choice of center avoids symmetry of the domain with respect to the partially shown computational grid ( $h = 0.025$ ). On the outer boundary, a displacement in the normal direction of length  $s$  is indicated by the dashed circle. The displacement on the traction-free inner boundary is indicated by the heavy circle.

## 6. NUMERICAL EXAMPLES

The examples in this section treat three different issues.

1. Our implementation of the Explicit Jump Immersed Interface Method for the Lamé equations finds displacements with second order accuracy on arbitrary domains with displacement and traction boundary conditions.
2. With a Schur-complement technique, the fast solver for rectangles from [33] can be used for problems on irregular domains as well. Our implementation scales like  $\mathcal{O}(N \log N)$ , just as the solver for rectangles.
3. The narrow band level set method can be used to alter the shape and topology of the structure, with velocities depending on the stresses in the current design. We recover the solution of a well-studied short cantilever example and show that our rules of stress and weight reducing design lead to truss-like structures.

**6.1. Second order convergence for the Lamé equations.** The following radially symmetric example was first studied in the pure loading case by Lamé which can also be found in the books by Murnaghan[17] and Timoshenko [30].

Consider (1) and (2) on the annulus  $r_1 < r < r_2$ ; see Figure 9. Clearly

$$u = \frac{sr_1(C(x^2 + y^2) + r_2^2)}{(r_2^2 + Cr_1^2)(x^2 + y^2)}x,$$

$$v = \frac{sr_1(C(x^2 + y^2) + r_2^2)}{(r_2^2 + Cr_1^2)(x^2 + y^2)}y,$$



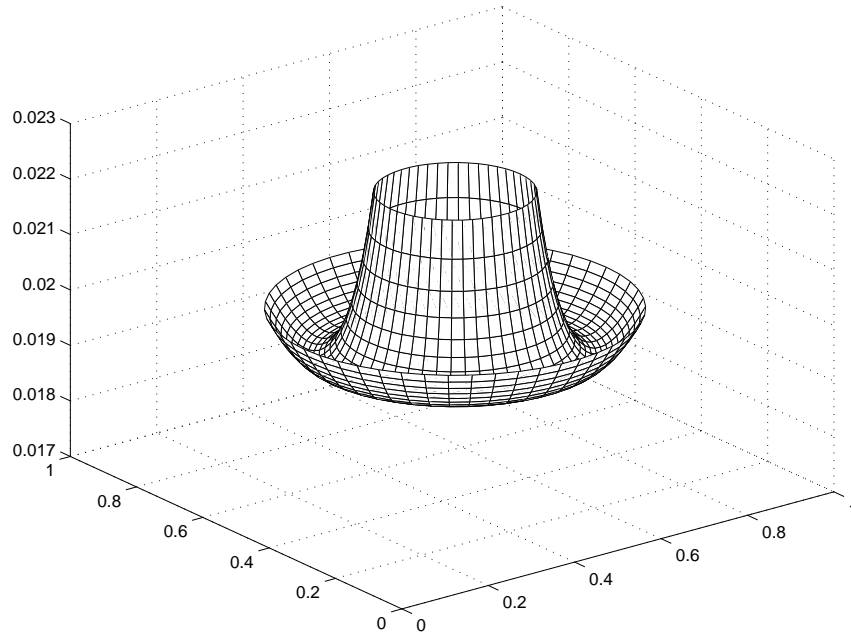


FIGURE 10. Wire frame of the length of displacement of the exact solution (for  $C = 1/3$ ,  $r_1 = 0.35$ ,  $r_2 = 0.15$ ,  $s = 0.02$  centered at  $(0.503, 0.495)$ ) evaluated on a polar grid.

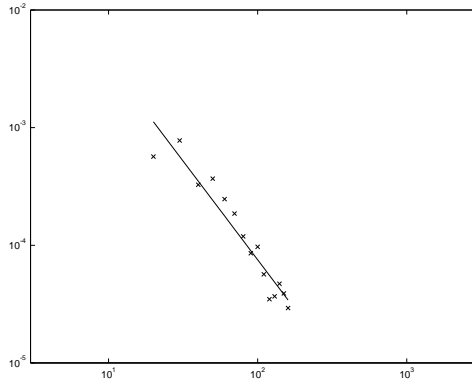


FIGURE 11. The maximum error over the displacements for  $n = 20, 30, 40, \dots, 160$ . The affine least squares fit indicates convergence with  $\mathcal{O}(h^{1.7})$ . Here the original 6 point stencil selection (see [35]) was used. The scatter shows significant influence of the mesh-boundary geometry.

satisfy the elastostatic equations (1), (2) with  $f^u = f^v = 0$ . The displacements  $u$  and  $v$  also satisfy displacement boundary conditions (3)

$$u = \frac{s}{r_1}x,$$

$$v = \frac{s}{r_1}y,$$

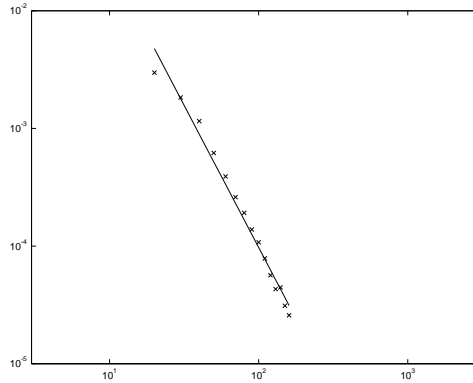


FIGURE 12. *Maximum error as in Figure 11, but for bi-quadratic least squares interpolation. The affine least squares fit indicates convergence with  $\mathcal{O}(h^{2.4})$ . The scatter of the errors is significantly reduced.*

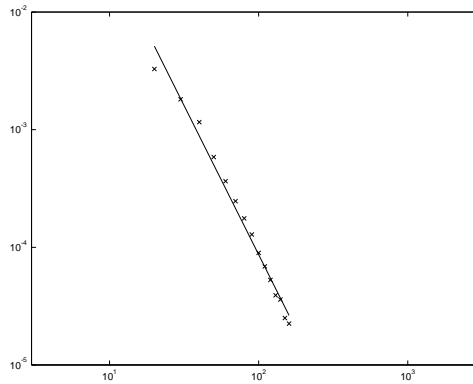


FIGURE 13. *Maximum error as in Figure 11, but for bi-cubic least squares interpolation. The affine least squares fit indicates convergence with  $\mathcal{O}(h^{2.5})$ , slightly better than for the bi-quadratic fit.*

on the inner boundary  $\{x^2 + y^2 = r_1^2\}$  and a traction free boundary condition ((4) with  $\mathbf{g} = 0$ ) on the outer boundary  $\{x^2 + y^2 = r_2^2\}$ .

Figure 10 shows the analytic solution (for  $s = 0.02$ ,  $r_1 = 0.35$ ,  $r_2 = 0.15$  and  $C = 1/3$ ; on a polar grid for visualization only). To test how well we can recover the symmetry of the solution on a Cartesian grid, we have shifted the origin to the point  $(0.503, 0.495)$ . The computational grids are uniformly spaced with  $n - 1$  interior grid points and meshwidth  $h = 1/n$  in the unit square  $[0, 1] \times [0, 1]$ .

Figure 11–13 display values for the maximum error of the displacement over all grid points inside the annulus as the mesh is refined, with  $n = 20, 30, 40, \dots, 160$  points in each direction. Figure 11 shows results for the original 6 point stencil selection scheme, Figure 12 shows results for bi-quadratic weighted least squares extrapolation and Figure 13 shows the results for bi-cubic weighted least squares extrapolation. We observe second order reduction of the error in the maximum norm in all figures, but a much more uniform behavior for the least squares fit, with slightly better results for the cubic fit. Figure 14 contains scatter plots that show the length of displacement as a function of the distance

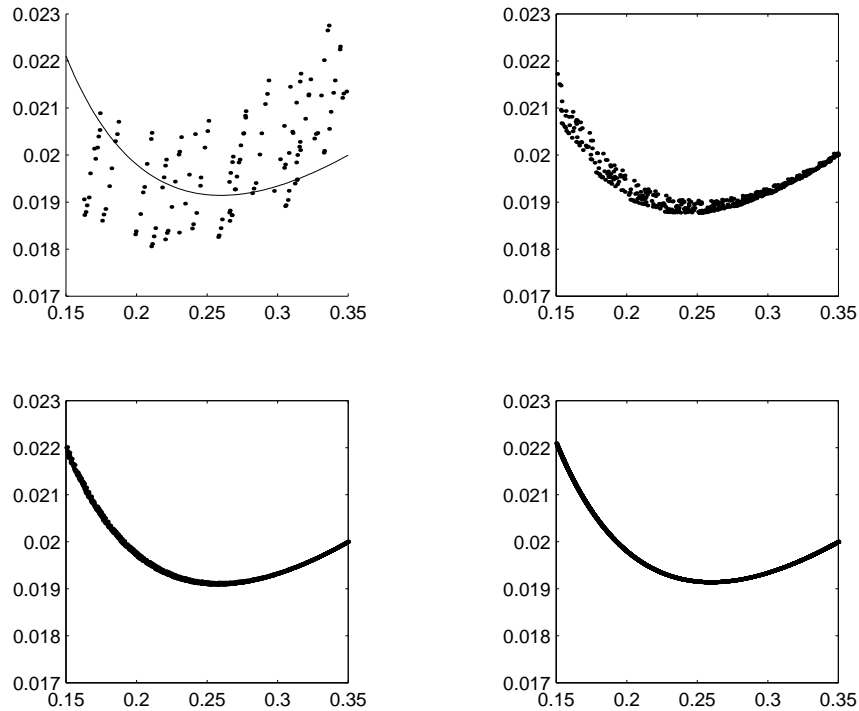


FIGURE 14. Scattering of length of displacement values for  $n = 20$ ,  $n = 40$ ,  $n = 80$  and  $n = 160$ . The first plot also shows the exact solution as a function of the radius. As the grid is refined, the symmetry of the exact solution is fully recovered.

of a grid point from the point  $(0.503, 0.495)$ . As the grid is refined for  $n = 20, 40, 80, 160$ , the radial symmetry of the solution is recovered.

**6.2. The  $\mathcal{O}(N \log N)$  solution method.** The fast solver that is outlined in §4.6 is used to apply  $A^{-1}$  in the Schur-complement inside GMRES or BiCGSTAB iterations. For large problems and/or high required accuracy, we find that BiCGSTAB is preferable because it requires less memory and the convergence of restarted GMRES is not very fast. However, because  $A^{-1}$  is applied four times per BiCGSTAB iteration and only once per GMRES iteration, for problems that we can solve with GMRES without restarting, GMRES is the preferred method.

Figure 2 shows the stress contour lines of an elastic structure that is loaded and clamped as indicated in Figure 1. The perforated rectangle is embedded in a larger rectangle, the computational domain, which is indicated in light gray in both figures. The same problem was solved on grids with  $40 \times 80$ ,  $80 \times 160$ ,  $160 \times 320$ ,  $320 \times 640$  and  $640 \times 1280$  points. The stresses in Figure 2 were found on the  $160 \times 320$  grid, but on the other grids the results were similar, with convergence under refinement. Because the largest problem requires BiCGSTAB in order to reside in the memory of our SUN workstation without swapping, we have used it even for the smaller problems where GMRES would apply in order to be able to compare the results. Table 1 establishes that also on irregular domains the operations and time required to solve the problem scale like  $\mathcal{O}(N \log N)$  and that we can use this method to solve medium sized problems on workstations. For each problem size, we have reduced the residue by six orders of magnitude. This ensured that the number

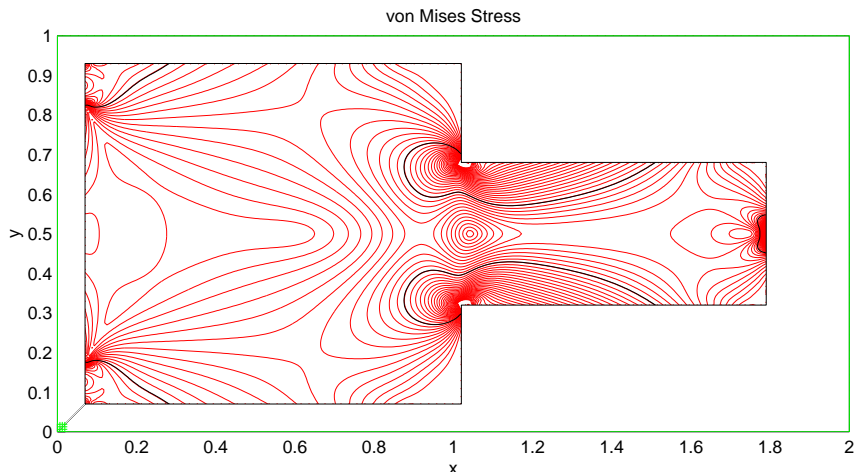


FIGURE 15. *Stress contours in the initial design. The dark curves represent the 20% contour of the maximal initial stress.*

of iterations was similar for all problems sizes and that we can compare the amount of work performed. In order to really benefit from the higher resolution, one should reduce the residue even further for the larger problems. The odd numbers of interior grid points were chosen to be able to compare point values with the finest grid. This means that the prime factorizations and hence the efficiency of the FFT vary, but growth like  $\mathcal{O}(N \log N)$  is observable nonetheless.

TABLE 1. *Performance of BiCGSTAB for the structure in Figure 2.*

$N$	Iterations	Flops	Flop Ratio	Mflops	Seconds	Time Ratio
$39 \times 79 \times 2$	36	2.7e09	—	77	3.5e1	—
$79 \times 159 \times 2$	49	3.4e10	12.6	148	2.3e2	6.6
$159 \times 319 \times 2$	48	1.8e11	5.3	164	1.1e3	4.8
$319 \times 639 \times 2$	60	6.8e11	3.8	145	4.7e3	4.3
$639 \times 1279 \times 2$	81	4.4e12	6.5	126	3.5e4	7.4

### 6.3. Structural Boundary Design via Level Set and Immersed Interface Method.

6.3.1. *Stress, weight and compliance reduction.* The cantilever in Figure 15 is clamped and loaded in the same fashion as indicated in Figure 1. High stresses occur at the inner endpoints of the clamped boundary portions and at the inward corners. This behavior is typical in elasticity, and the rounding of such corners is known as filleting.

Here, we show that our approach is able to find good fillets while at the same time reducing the compliance and the weight of the structure. We do not claim to reach an optimum, but believe that the reduction of the maximal stress at the fillet by 60%, reduction of compliance by 20% and reduction of weight by 10% together with the simplicity of the design rules are practically relevant.

As the homotopy parameter, we have arbitrarily chosen  $\bar{\sigma}$  as 20% of the maximal von Mises stress in the initial design in Figure 15. The corresponding contour is fattened in Figure 15—Figure 17. We allow outward motion (i.e. for stress above  $\bar{\sigma}$ ) in a neighborhood of the initial corners, and cut one hole along a contour of low stress. This hole is then allowed to grow on portions of its boundary that are stressed below  $\bar{\sigma}$ . In principle, the

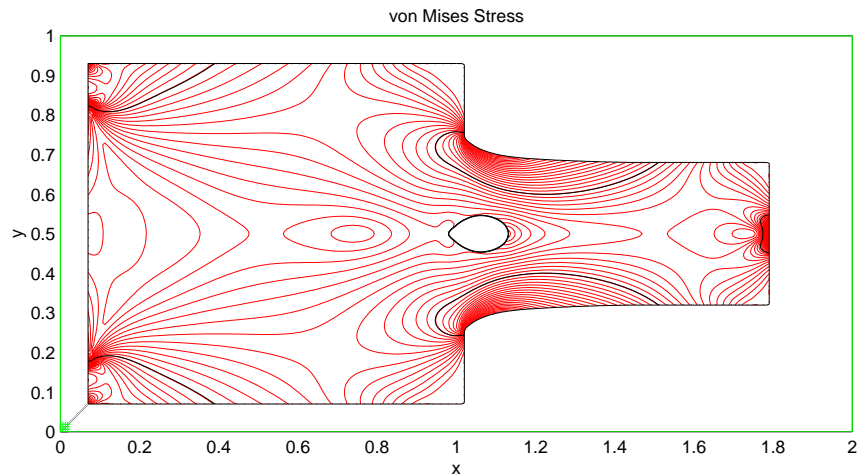


FIGURE 16. The formation of the fillet for the design in Figure 15 is essentially finished, the hole is still growing. This growth drives further changes of the fillet. The dark curves represent the 20% contour of the maximal initial stress.

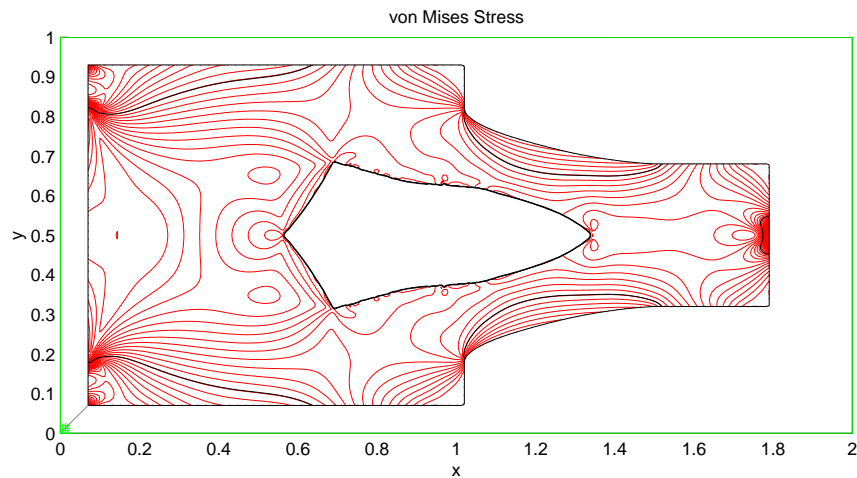


FIGURE 17. Formation of fillet and hole are finished. The dark curves represent the 20% contour of the maximal initial stress.

hole could shrink as well, but the stresses on its boundary do not reach the point where shrinking would occur. Cutting the hole allows us to design a cantilever with less weight than the original one even though we add material in the corners.

After 10 design steps, with shape seen in Figure 16, the stress in the fillets has been reduced by 50%. Now the growth of the hole drives further changes in the fillet shape until that also stabilizes at the shape in Figure 17. The fillet shape that develops is similar to that found by Xie and Stevens [36], but note that we achieve it by the opposite procedure. Rather than removing material from a ground structure, we add material where the stresses are high. Also, the stress contours are much smoother in the final

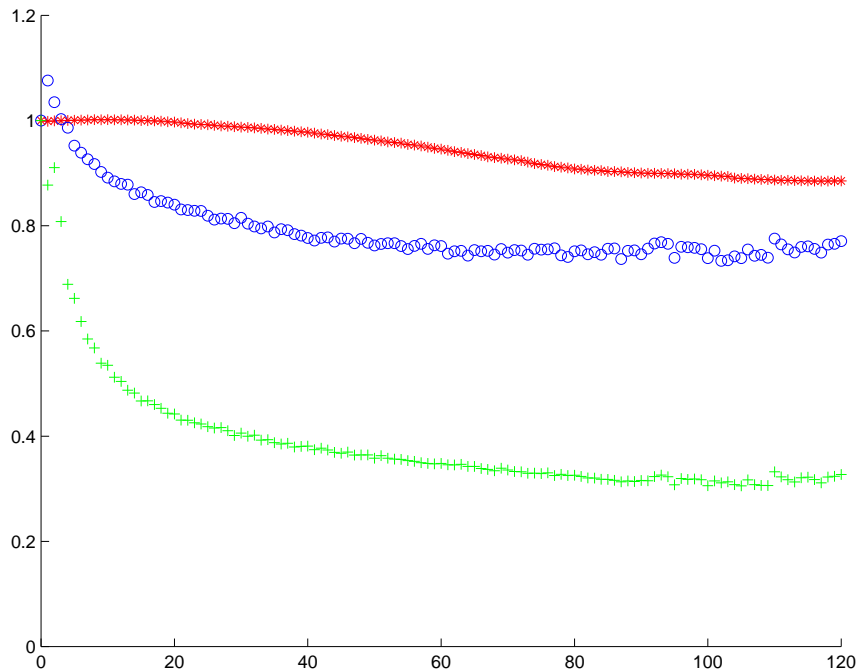


FIGURE 18. *Maximal stress (crosses), compliance (circles) and weight (stars) for the fillet design example from Figure 15—Figure 17.*

design than in the initial design. On the down side, at the inner endpoints of the clamped boundaries, the stress has increased by 25%.

Figure 18 shows the behavior of the maximal stress (maximum taken away from the clamped and loaded boundary portions), weight and compliance. They are all scaled to one at the initial design. The oscillations in the compliance and stress for the later designs are due to a “ripple motion” as parts of the hole boundary are stressed close to the limit of outward motion.

**6.3.2. Constrained design of a short cantilever.** A cantilever of ratio 1:3 is clamped everywhere on the left boundary and vertically loaded on the mid 6% of the right boundary. The rest of the right boundary and the top and bottom boundaries are traction free, as indicated in Figure 19.

This problem was chosen because it is a standard test problem for structural boundary design (used e.g. in [36, 20]), with a known solution for a simpler pin-jointed two-truss problem [21]. The optimal height in that case is twice the width of the structure.

Figure 19 a) also shows the distribution of the von Mises stress in the original design. Figure 19 b) shows an improved geometry close to the two-truss solution and stress distribution inside. We have almost achieved a fully stressed design. Except for the left, built in edge, the cantilever is stressed to at least 40% of the maximal stress of the initial design.

We consider the problems of improving the weight of the cantilever for three different constraints on the compliance. The constraints are 1.2, 2.0 and 10.0 times the compliance of the “full” design from Figure 19. Improved designs are seen in Figure 20 a), b) and c), respectively. It is clear that the shape depends very much on the constraint, and a more lenient constraint allows the use of less material.

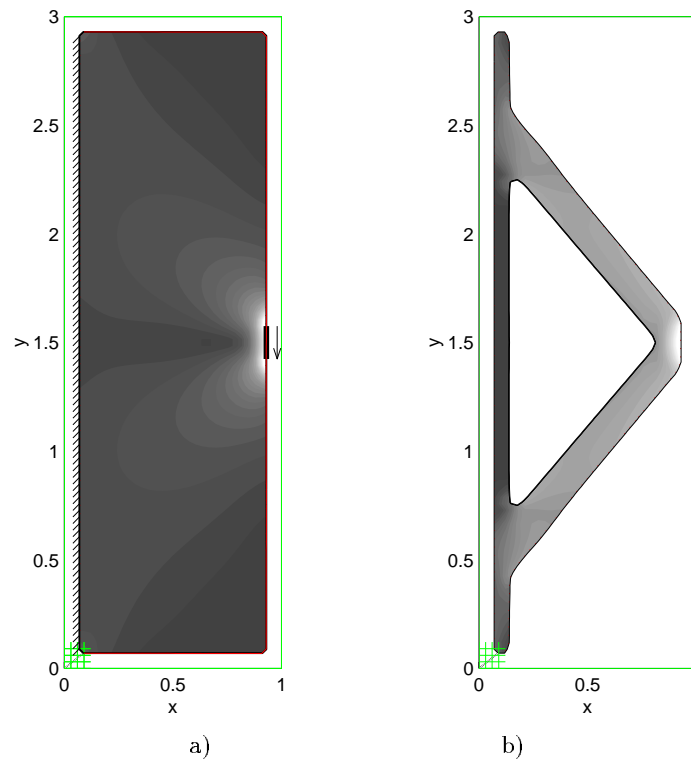


FIGURE 19. a) Clamping, loading and stresses in the initial design. b) Stress distribution in an improved design close to the pin-jointed two-truss solution.

Figure 21 a) shows the evolution of the weight (circles) and compliance (crosses) for the constraint at 2.0. Simple control of the homotopy parameter based on constraint violation leads to a non-monotone decrease of the weight, but allows significant changes in shape when the constraint is reached and the homotopy parameter is decreased.

Figure 21 b) shows the number of GMRES iterations needed for the different designs. The iteration count is always in the same range, with a slight increase as the geometry of the design becomes more complicated.

6.3.3. *Design of a long cantilever from a perforated structure.* A cantilever of ratio 2:1 is built in near the top and bottom of the left edge and centrally loaded on 5% of the right hand edge. The rest of the right hand edge and the top and bottom edges are traction free. From theoretical considerations [4, 7], a truss like structure is expected to develop for optimal low weight structures in these conditions. These solutions have been observed based on a rectangular ground structure both in homogenization, where a weighted sum of weight and compliance are minimized [5], and in evolutionary structural optimization, where material below a certain stress level is removed [21, 36]. Using unconstrained weight reduction by homotopy on the stress, we observe the same phenomenon based on a perforated ground structure. The homotopy parameter is initially rather small, so that the small holes tend to disappear. After the stable configuration in Figure 29 is reached, the homotopy parameter is increased slowly and a truss-like structure develops as more material is removed.

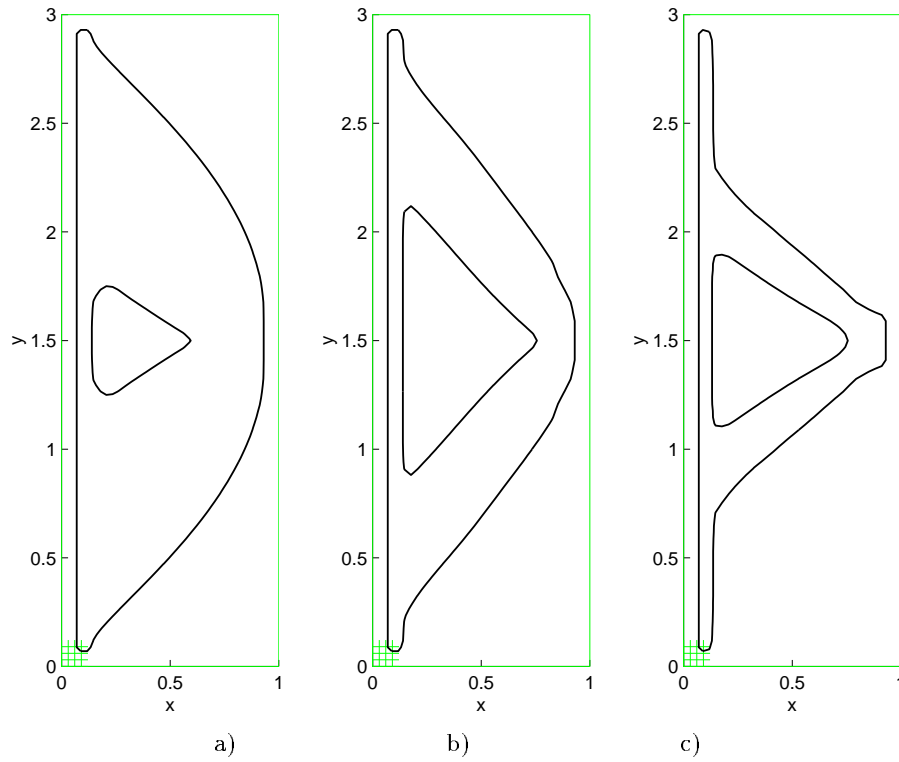


FIGURE 20. Improved designs for various constraints on the compliance. a) 1.2, b) 2.0 and c) 10 times the compliance of the initial design in Figure 19.

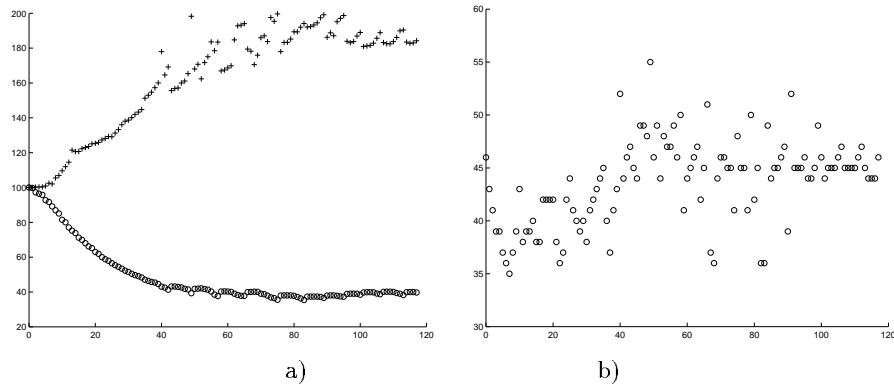


FIGURE 21. a) Compliance (crosses) and weight (circles) of the sequence of designs leading to the one in Figure 20 b). b) Number of GMRES iterations needed to find the stresses in the designs leading to the one in Figure 20 b).



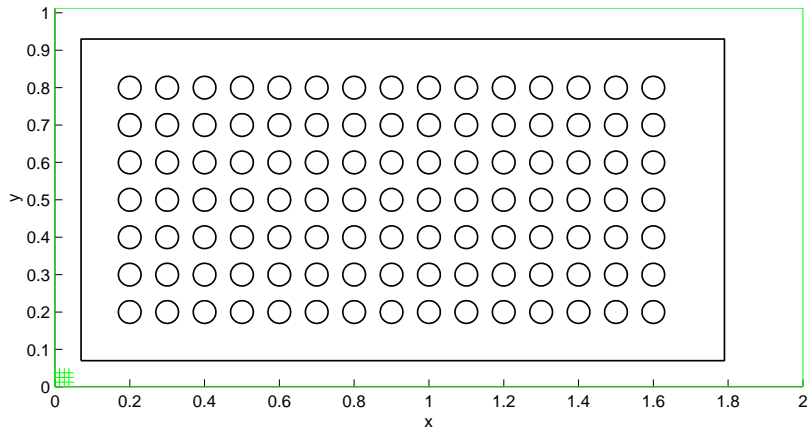


FIGURE 22. *Initial Design.*

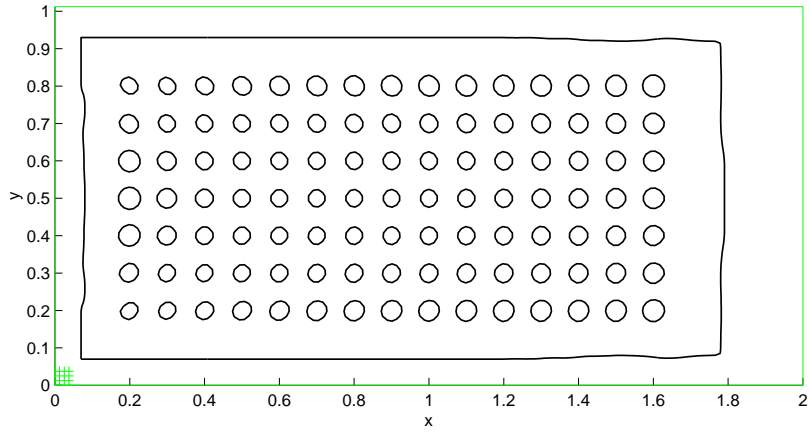


FIGURE 23. *Design 1.*

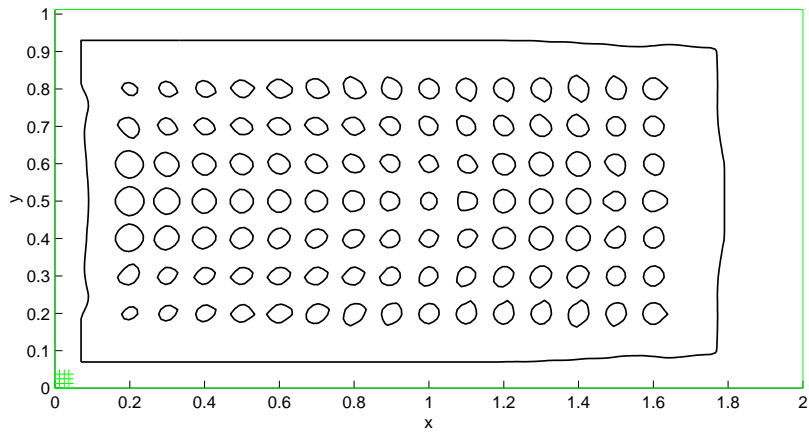
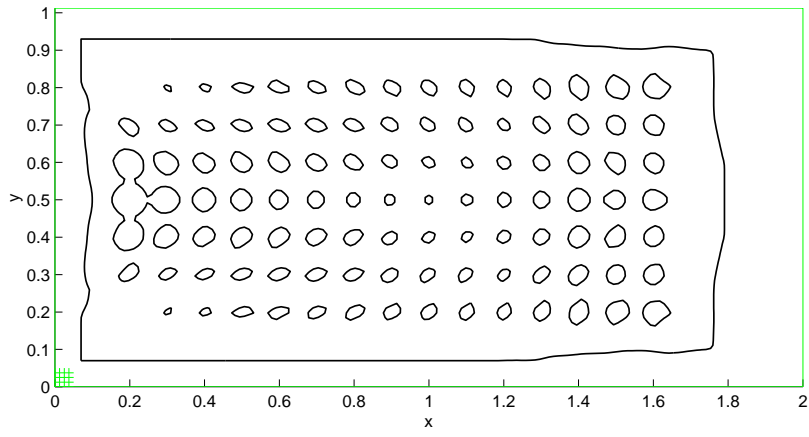
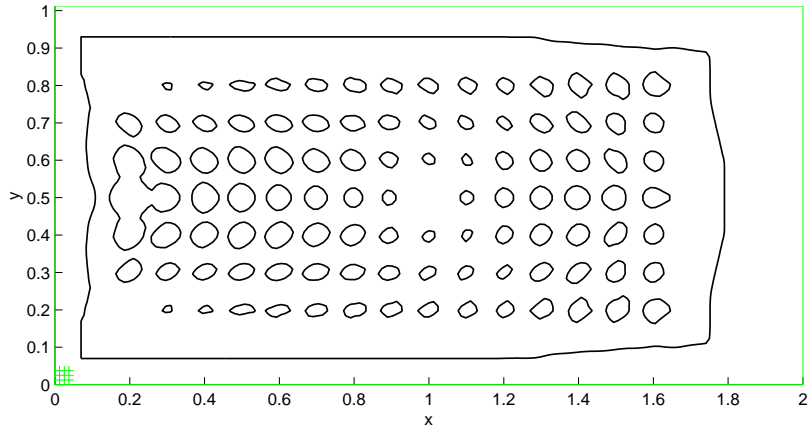
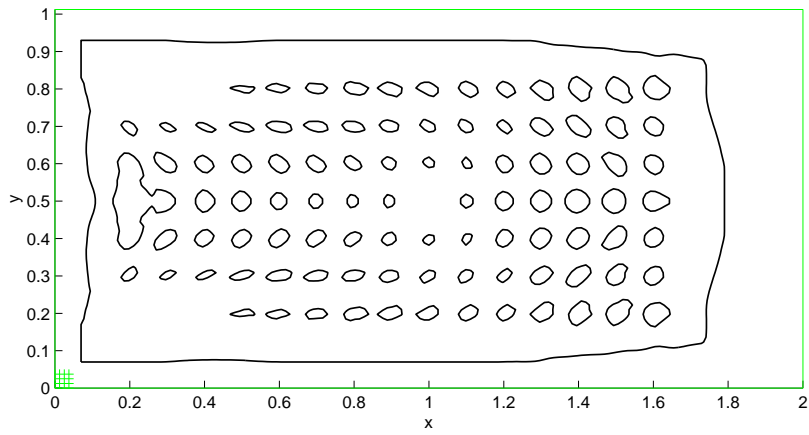


FIGURE 24. *Design 2.*

FIGURE 25. *Design 3.*FIGURE 26. *Design 4.*FIGURE 27. *Design 5.*

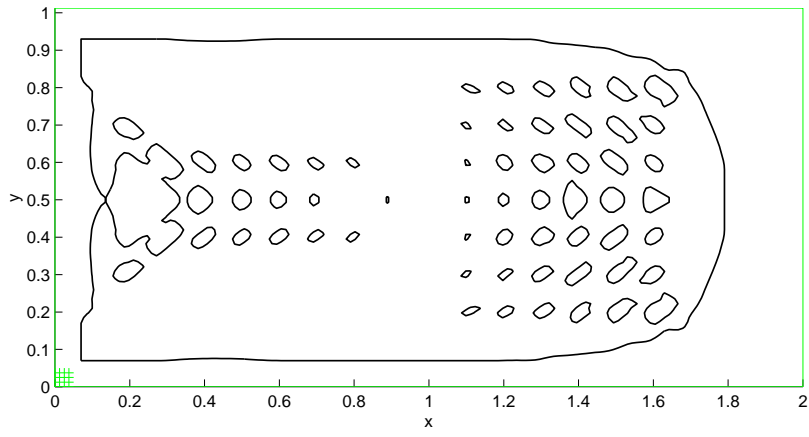


FIGURE 28. *Design 10.*

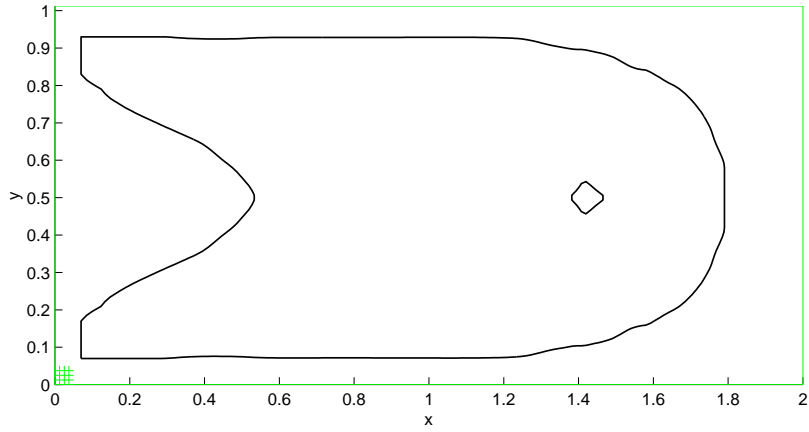


FIGURE 29. *Design 30.*

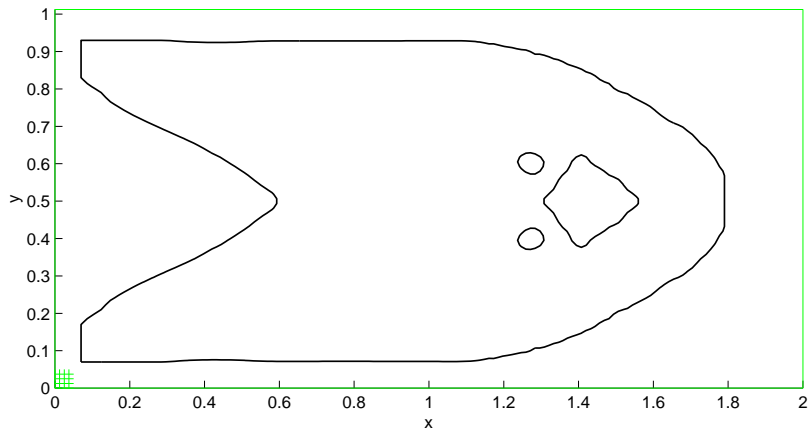
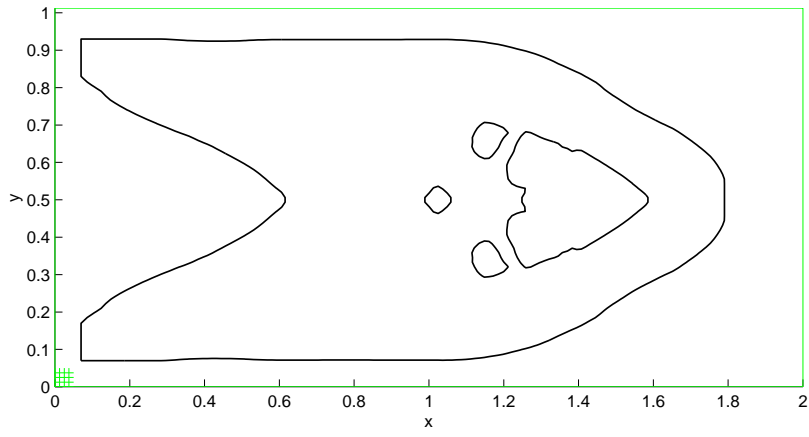
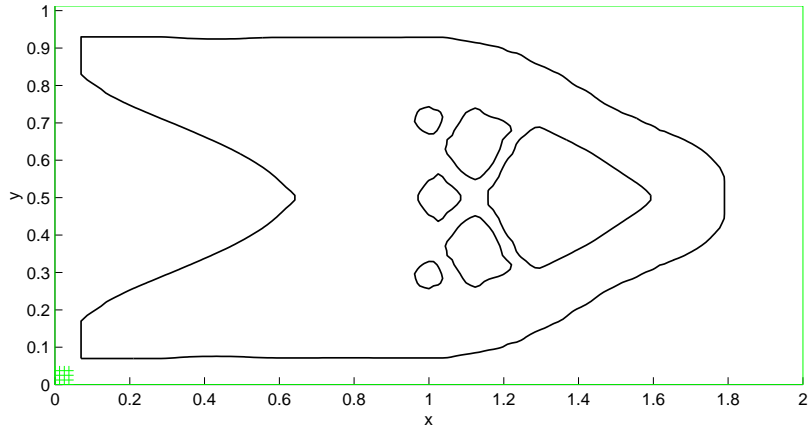
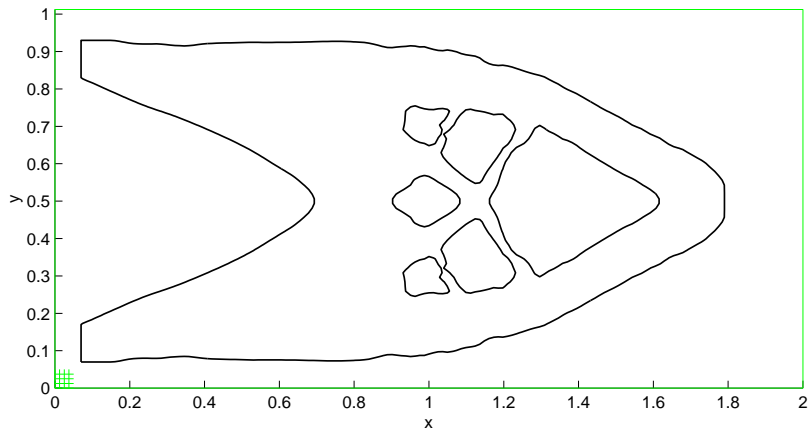
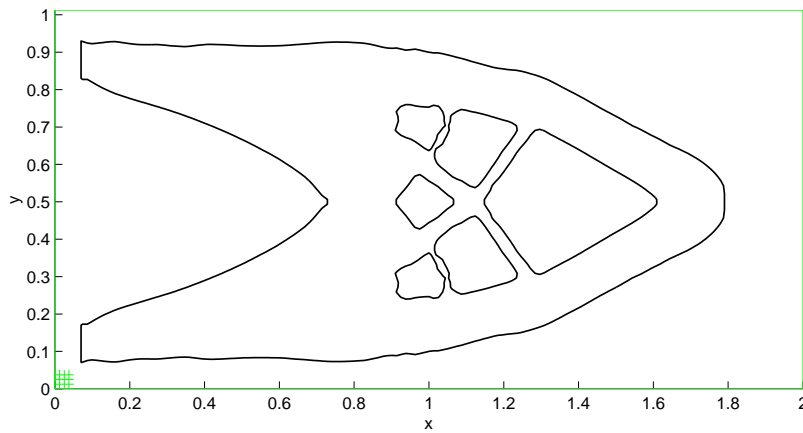
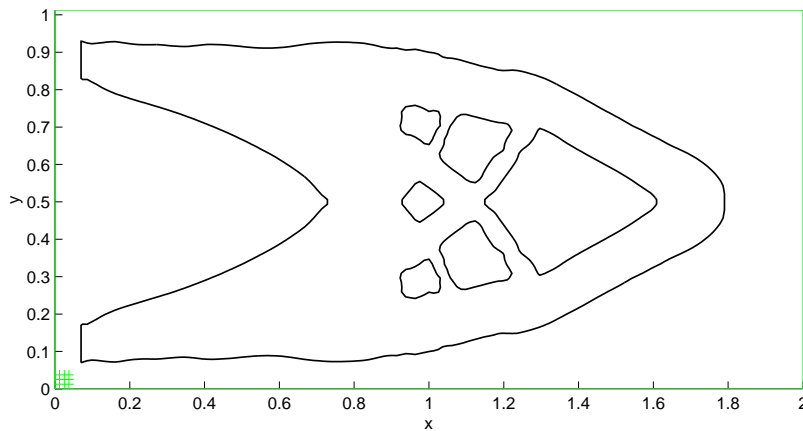


FIGURE 30. *Design 50.*

FIGURE 31. *Design 70.*FIGURE 32. *Design 90.*FIGURE 33. *Design 110.*

FIGURE 34. *Design 130.*FIGURE 35. *Design 135.*

## 7. CONCLUSION AND OUTLOOK

We have presented a numerical algorithm for structural boundary design. The technique accurately solves the Lamé equations and accurately differences the displacements for the stresses in arbitrary domains. It can be used to find basically optimal solutions to constrained minimization problems in some simple, well-studied test cases. We expect to extend the work to three dimensions and more complex situations. A large collection of case studies and further refinements may be found in [29].

## 8. ACKNOWLEDGMENTS

The authors thank A. Sarti, D. Adalsteinsson and D. Kessler for their comments and suggestions. Valerie Heatlie helped with typesetting parts of this paper. All calculations were performed at the Lawrence Berkeley National Laboratory. A web page describing level set and Fast Marching Methods may be found at <http://www.math.berkeley.edu/~sethian>

## REFERENCES

- [1] D. Adalsteinsson and J. A. Sethian. A fast level set method for propagating interfaces. *Journal of Computational Physics*, 118(2):269—277, 1995.
- [2] D. Adalsteinsson and J. A. Sethian. The Fast Construction of Extension Velocities in Level Set Methods. *Journal of Computational Physics*, 148:2—22, 1999.
- [3] G. Allaire. The homogenization method for topology and shape optimization. In G. I. N. Rozvany, editor, *Topology Optimization in Structural Mechanics*, pages 101—133. CISM, 1997.
- [4] G. Allaire and R. V. Kohn. Optimal design for minimum weight and compliance using extremal microstructures. *European Journal of Mechanics A/Solids*, 12:839—878, 1993.
- [5] G. Allaire and R. V. Kohn. Topology optimization and optimal shape design using homogenization. In M. P. Bendsøe and C. A. Mota Soares, editors, *Topology Design of Structures*, volume 227 of *NATO ASI Series, Series E*, pages 207—218. Kluwer, 1993.
- [6] M. P. Bendsøe. *Optimization of Structural Topology, Shape and Material*. Springer: Berlin, 1997.
- [7] M. P. Bendsøe and R. Haber. The Michell layout problem as a low volume fraction limit of the homogenization method for topology design: an asymptotic study. *J. Structural Optimization*, 6:263—267, 1993.
- [8] M. P. Bendsøe and N. Kikuchi. Generating optimal topologies in structural design using a homogenization method. *Computer Methods in Applied Mechanics and Engineering*, 71:197—224, 1988.
- [9] B. L. Buzbee, F. W. Dorr, J. A. George, and G. H. Golub. The direct solution of the discrete Poisson equation on irregular regions. *SIAM J. Numer. Anal.*, 8(4):722—736, 1971.
- [10] S. Chen, B. Merriman, S. Osher, and P. Smereka. A Simple Level Set Method for Solving Stefan Problems. *Journal of Computational Physics*, 138:8—29, 1997.
- [11] D. L. Chopp. Computing Minimal Surfaces via Level Set Curvature Flow. *Journal of Computational Physics*, 106:77—91, 1993.
- [12] H. A. Eschenauer, H. A. Kobleev, and A. Schumacher. Bubble method for topology and shape optimization of structures. *J. Structural Optimization*, 8:142—151, 1994.
- [13] H. A. Eschenauer and A. Schumacher. Topology and shape optimization procedures using hole positioning criteria. In G. I. N. Rozvany, editor, *Topology Optimization in Structural Mechanics*, pages 135—196. CISM, 1997.
- [14] R. J. LeVeque and Z. Li. The Immersed Interface Method for Elliptic Equations with Discontinuous Coefficients and Singular Sources. *SIAM J. Numer. Anal.*, 31:1019—1044, 1994.
- [15] Z. Li. A Fast Iterative Algorithm for Elliptic Interface Problems. *SIAM J. Numer. Anal.*, 35(1):230—254, 1998.
- [16] R. A. Lorentz. *Multivariate Birkhoff Interpolation*. Springer, 1992.
- [17] F. D. Murnaghan. *Finite deformation of an elastic solid*. New York, Wiley, 1951.
- [18] S. J. Osher and J. A. Sethian. Fronts propagating with curvature dependent speed: Algorithms based on the Hamilton-Jacobi formulation. *Journal of Computational Physics*, 79:12—49, 1988.
- [19] W. Proskurovski and O. Widlund. On the Numerical Solution of Helmholtz's Equation by the Capacitance Matrix Method. *Math. Comp.*, 30(135):433—468, 1976.
- [20] D. Reynolds, J. McConnachie, P. Bettess, W. C. Christie, and J. W. Bull. Reverse adaptivity—a new evolutionary tool for structural optimization. *Int. J. Numer. Meth. Engng.*, 45:529—552, 1999.
- [21] G. I. N. Rozvany, M. P. Bendsøe, and U. Kirsch. Layout optimisation of structures. *Applied Mechanics Review*, 48(2):41—119, 1995.
- [22] Y. Saad and M. H. Schultz. GMRES: A generalized minimal residual Algorithm for solving nonsymmetric linear systems. *SIAM J. Sci. Statist. Comput.*, 7(3):856—869, 1986.
- [23] J. A. Sethian. *An Analysis of Flame Propagation*. PhD thesis, Dept. of Mathematics, University of California, Berkeley, CA, 1982.
- [24] J. A. Sethian. Curvature and the Evolution of Fronts. *Comm. in Math. Phys.*, 101:487—499, 1985.
- [25] J. A. Sethian. Numerical Methods for Propagating Fronts. In P. Concus and R. Finn, editor, *Proceedings of the 1985 Vallambrosa Conference, Variational Methods for Free Surface Interfaces*, 155—164, Springer-Verlag, NY, 1987.
- [26] J. A. Sethian. A fast marching level set method for monotonically advancing fronts. *Proc. Nat. Acad. Sci.*, 93(4):1591—1595, 1996.
- [27] J. A. Sethian. *Level set methods: Evolving interfaces in geometry, fluid mechanics, computer vision, and material science*. Cambridge University Press, 1996.
- [28] J. A. Sethian. *Level set methods and Fast Marching Methods: Evolving interfaces in computational geometry, fluid mechanics, computer vision, and materials sciences*. Cambridge University Press, 1999.
- [29] J. A. Sethian and A. Wiegmann, Construction of Efficient Designs through Evolving Interfaces *Int. J. Numer. Meth. Engng.*, to be submitted for publication, 1999.
- [30] S. Timoshenko. *Theory of elasticity*. New York, McGraw-Hill, 3d edition, 1970.
- [31] H. A. van der Vorst. Bi-CGSTAB: A fast and smoothly converging variant of Bi-CG for the solution of nonsymmetric linear systems. *SIAM J. Sci. Statist. Comput.*, 13:631—644, 1992.
- [32] A. Wiegmann. *The Explicit-Jump Immersed Interface Method and Interface Problems for Differential Equations*. PhD thesis, University of Washington, 1998.
- [33] A. Wiegmann. Fast Poisson, fast Helmholtz and fast linear elastostatic solvers on rectangular parallelepipeds. Technical Report LBNL-43565, Lawrence Berkeley National Laboratory, MS 50A-1148, One Cyclotron Rd, Berkeley CA 94720, June 1999. Submitted to *SIAM J. Scientific Computing*.
- [34] A. Wiegmann. Improved scaling in 2D and 3D for reflection based fast solvers. In preparation, November 1999.

- [35] A. Wiegmann and K. P. Bube. The Explicit–Jump Immersed Interface Method: Finite Difference Methods for PDE with piecewise smooth solutions. To appear in *SIAM J. Numer. Anal.*
- [36] Y. M. Xie and G. P. Steven. *Evolutionary Structural Optimization*. Springer, 1997.
- [37] Z. Yang. *A Cartesian Grid Method for Elliptic Boundary Value Problems in Irregular Regions*. PhD thesis, University of Washington, 1996.  
*E-mail address:* `wiegmann@math.berkeley.edu`, `sethian@math.berkeley.edu`  
*URL, J.A.Sethian:* `http://www.math.berkeley.edu/~sethian`  
*URL, Andreas Wiegmann:* `http://math.lbl.gov/~wiegmann`